Chapter X

CHAPTER X

PHYSICOCHEMICAL STUDY, THERMAL BEHAVIOR AND APPLICATION OF TRANSITION METAL COMPLEXES OF GUANIDINIUM -2-NAPHTHOATE

10.1 INTRODUCTION

Guanidine has five possible donor sites for hydrogen bonding interactions. Heteroaromatic guanidinium salts have been successfully used as building blocks for the complexes due to their strong hydrogen bond [1]. The prepared complexes were characterized by element analysis, FTIR, electronic spectra, thermal analysis, and P-XRD. The complexes reveal good antimicrobial and antioxidant activity. The photometric properties of the complexes were studied by PL analysis, CIE, and CCT and found to be suitable phosphors for OLEDs. The prepared complexes were calcinated at 700°C to form metal oxide as final residue. To study the corrosion behavior, the nanometal and mixed metal oxide namely $CeMnO_3$, CeO, and MnO was synthesized and coated along with epoxy resin on the steel substrate. The structural parameters and surface morphology were determined from XRD, SEM, and TEM analysis. The results were deliberated in this chapter X.

10.2 EXPERIMENTAL

10.2.1. Synthesis method

The complexes were prepared by adding appropriate amount of 2-naphthoic acid and guanidine hydrochloride in 40 ml Milli- Q water and subsequently a clear solution of the metal nitrate ion was added and kept in a water bath for 8 hours and cooled. The microcrystalline solid obtained was dried in the desiccator. This schematic representation for the synthesis step is shown in **Figure 10.1**.

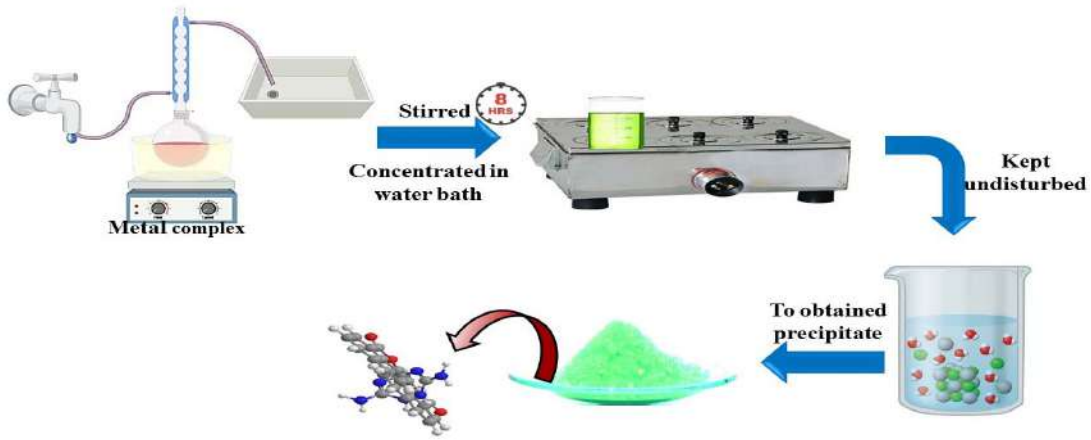

Figure 10.1 *Synthesis of metal complexes*

10.3 RESULTS AND DISCUSSION

10.3.1 Analytical Data

The predicted data, which were examined with the elemental analysis and analytic data represented in **Table 10.1** and **10.2**.

Table 10.1 *Analytical data*

Metal Complexes	Molecular weight (g/mol)	Color	pH	Melting point (oC)	Metal (%)	
					Found	Calc
$[Mn(CH_5N_3)_2\{C_{10}H_7(2COO)\}_2.2H_2O]$	550.45	Light pink	7	284	10.8	10.97
$[Co(CH_5N_3)_2\{C_{10}H_7(2COO)\}_2.2H_2O]$	554.44	Pink	6	274	10.3	10.4
$[Ni(CH_5N_3)_2\{C_{10}H_7(2COO)\}_2.2H_2O]$	554.20	Green	7	258	17.2	17.0
$[Cu(CH_5N_3)_2\{C_{10}H_7(2COO)\}_2.2H_2O]$	559.05	Blue	8	189	11.7	11.5
$[Zn(CH_5N_3)_2\{C_{10}H_7(2COO)\}_2.2H_2O]$	560.89	Dirty white	8	267	11.6	11.0
$[Cd(CH_5N_3)_2\{C_{10}H_7(2COO)\}_2.2H_2O]$	607.92	white	7	296	18.9	18.8

Metal Complexes	Molecular weight (g/mol)	Color	pH	Melting point (oC)	Metal (%)	
					Found	Calc
[Ca(CH_5N_3)$_2$ {$C_{10}H_7$(2COO)}$_2$.2H_2O]	539.53	White	7	278	7.4	7.3
[Sr(CH_5N_3)$_2$ {$C_{10}H_7$(2COO)}$_2$.2H_2O]	583.13	White	6	296	15.0	15.3
[Ba(CH_5N_3)$_2$ {$C_{10}H_7$(2COO)}$_2$.2H_2O]	632.83	White	6	258	12.7	12.8
[Mg(CH_5N_3)$_2$ {$C_{10}H_7$(2COO)}$_2$.2H_2O]	519.81	White	6	28	18.4	18.3

Table 10.2 *Elemental data*

Complexes	% Carbon Found (Cald)	% Hydrogen Found (Cald)	% Nitrogen Found (Cald)	% Oxygen Found (Cald)
[Mn(CH_5N_3)$_2$ {$C_{10}H_7$(2COO)}$_2$.2H_2O]	52.46 (52.00)	4.77 (4.71)	15.30 (15.05)	17.47 (17.39)
[Co(CH_5N_3)$_2$ {$C_{10}H_7$(2COO)}$_2$.2H_2O]	52.09 (52.01)	4.74 (4.70)	15.19 (15.13)	17.35 (17.31)
[Ni(CH_5N_3)$_2$ {$C_{10}H_7$(2COO)}$_2$.2H_2O]	52.11 (52.01)	4.74 (4.69)	15.19 (15.15)	17.35 (17.30)
[Cu(CH_5N_3)$_2$ {$C_{10}H_7$(2COO)}$_2$.2H_2O]	51.65 (51.60)	4.70 (4.69)	15.06 (15.03)	17.20 (17.19)
[Zn(CH_5N_3)$_2$ {$C_{10}H_7$(2COO)}$_2$.2H_2O]	51.49 (51.36)	4.68 (4.65)	15.01 (15.00)	17.15 (17.01)
[Cd(CH_5N_3)$_2$ {$C_{10}H_7$(2COO)}$_2$.2H_2O]	47.50 (47.49)	4.32 (4.30)	13.85 (13.87)	15.82 (15.80)

Complexes	% Carbon Found (Cald)	% Hydrogen Found (Cald)	% Nitrogen Found (Cald)	% Oxygen Found (Cald)
$[Ca(CH_5N_3)_2 \{C_{10}H_7(2COO)\}_2.2H_2O]$	53.92 (53.89)	4.90 (4.89)	15.72 (15.70)	17.96 (17.92)
$[Sr(CH_5N_3)_2 \{C_{10}H_7(2COO)\}_2.2H_2O]$	49.52 (49.50)	4.50 (4.49)	14.44 (14.40)	16.49 (16.40)
$[Ba(CH_5N_3)_2 \{C_{10}H_7(2COO)\}_2.2H_2O]$	45.62 (45.60)	4.15 (4.13)	13.30 (13.29)	15.19 (15.16)
$[Mg(CH_5N_3)_2 \{C_{10}H_7(2COO)\}_2.2H_2O]$	55.56 (55.50)	5.05 (5.03)	16.20 (16.19)	18.50 (15.49)

10.3.2 FT-IR analysis

The IR spectra of stretching frequencies υ (OH) indicate a peak around 3336-3587 cm^{-1} in all metal complexes. The presence of asymmetric and symmetric carboxylate ion was seen at 1568-1668 cm^{-1}. The N-H frequency was found around 1096-3300 cm^{-1}. The peak in the region 372-407 cm^{-1} peak confirms the formation of M-O bonding. This IR spectra of all synthesized metal complexes are represented in **Table 10.3** and **Figure 10.2**.

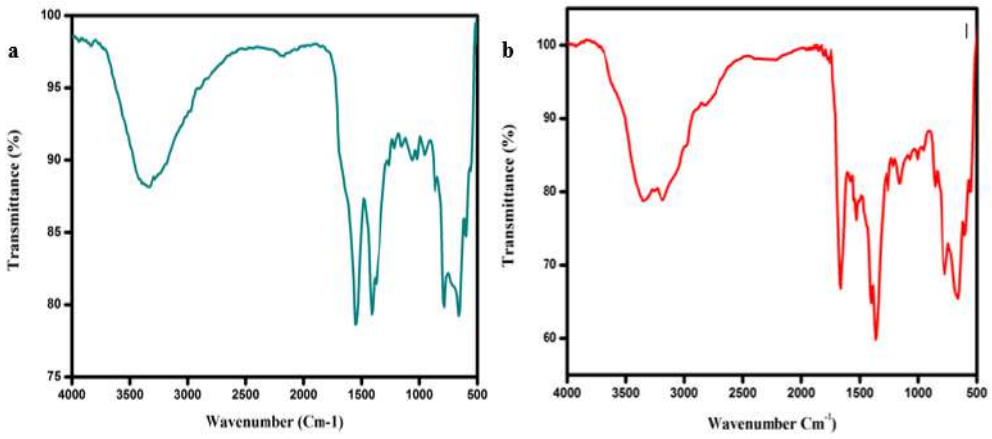

Figure 10.2 *FT-IR spectra a) Mn (II) b) Co(II) complex*

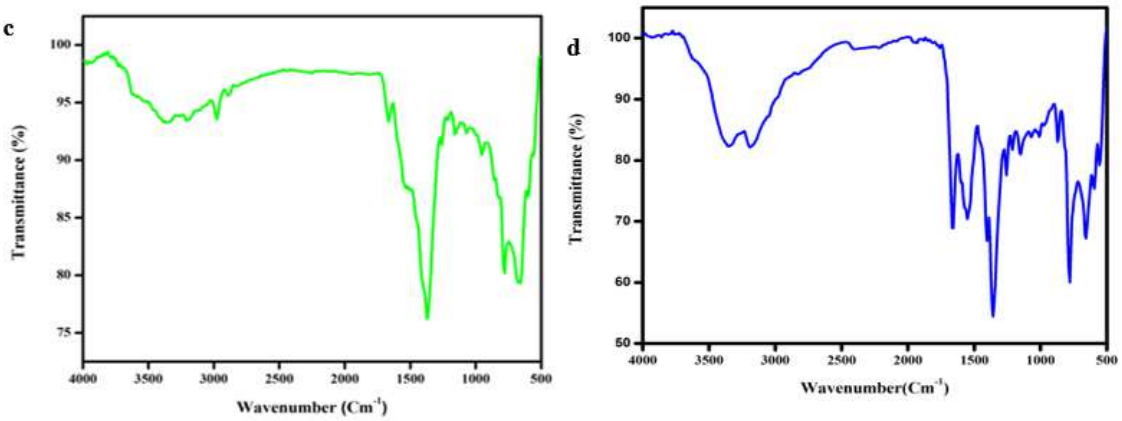

Figure 10.2 *FT-IR spectra c) Ni(II) d) Cu(II) complex*

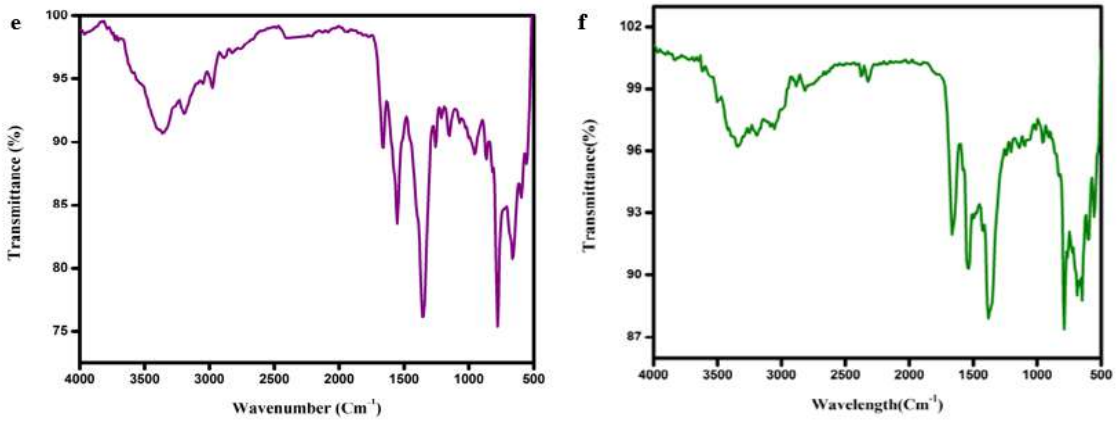

Figure 10.2 *FT-IR spectra e) Zn(II) f) Cd(II) complex*

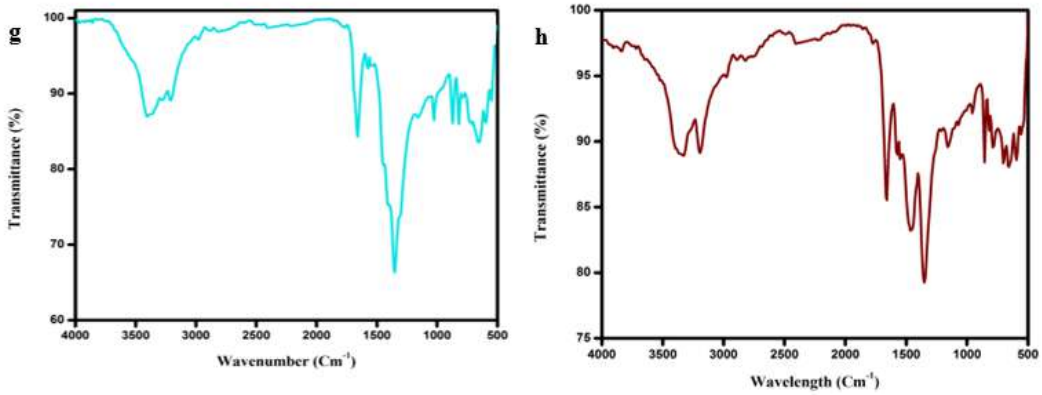

Figure 10.2 *FT-IR spectra g) Ca(II) h) Sr(II) complex*

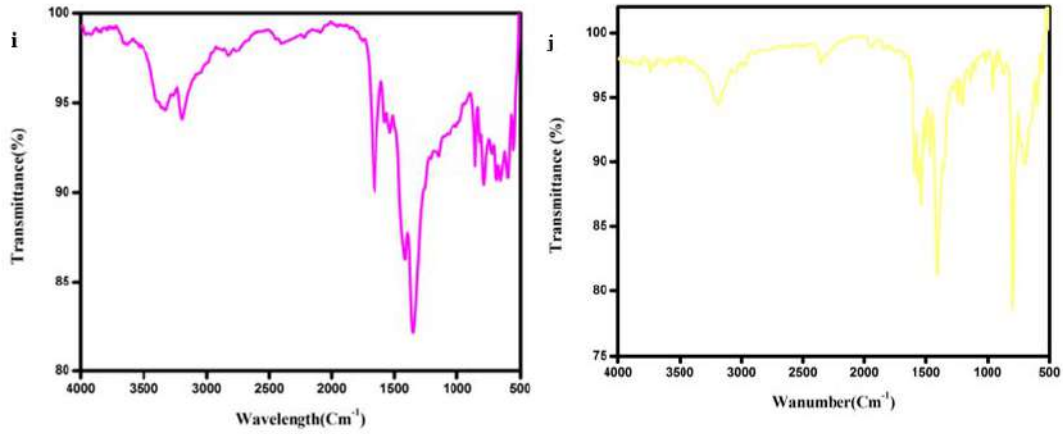

Figure10.2 *FT-IR spectra i) Ba(II) j) Mg(II) complex*

Table 10.3 *FT-IR Spectra.*

Complexes	υC=N cm^{-1}	υC=O sym cm^{-1}	υC=O asym cm^{-1}	υ asy-υsy cm^{-1}	υ M-O cm^{-1}	υ OH cm^{-1}	υ NH cm^{-1}
$[Mn(CH_5N_3)_2\{C_{10}H_7(2COO)\}_2.2H_2O]$	1221	1666	1345	321	398	3439	3358
$[Co(CH_5N_3)_2\{C_{10}H_7(2COO)\}_2.2H_2O]$	1216	1663	1377	86	407	3369	3233
$[Ni(CH_5N_3)_2\{C_{10}H_7(2COO)\}_2.2H_2O]$	1221	1660	1374	286	394	3424	3183
$[Cu(CH_5N_3)_2\{C_{10}H_7(2COO)\}_2.2H_2O]$	1214	1655	1367	288	379	3567	3377
$[Zn(CH_5N_3)_2\{C_{10}H_7(2COO)\}_2.2H_2O]$	1223	1628	1370	258	385	3435	3212
$[Cd(CH_5N_3)_2\{C_{10}H_7(2COO)\}_2.2H_2O]$	1221	1668	1368	300	402	3344	3190
$[Ca(CH_5N_3)_2\{C_{10}H_7(2COO)\}_2.2H_2O]$	1221	1749	1375	374	372	3380	3169
$[Sr(CH_5N_3)_2\{C_{10}H_7(2COO)\}_2.2H_2O]$	1289	1631	1352	279	394	3395	3051
$[Ba(CH_5N_3)_2\{C_{10}H_7(2COO)\}_2.2H_2O]$	1214	1639	1421	218	408	3519	3322
$[Mg(CH_5N_3)_2\{C_{10}H_7(2COO)\}_2.2H_2O]$	1229	1653	1375	278	372	3344	3205

10.3.3 Electronic spectra

Electronic spectra for the Ni(II) complex shows two bands at 250 nm and 300 nm due to $^{3}A2g(F) \rightarrow {}^{3}T1g$ (F) and $^{3}A2g(F) \rightarrow {}^{3}T1g$ (P) transitions. Co(II) complex shows band at 250 nm and 380 nm owing to $^{4}T1g$ (F) $\rightarrow {}^{4}A2g(F)$ and $^{4}T1g$ (F) $\rightarrow {}^{4}T2g$ (P) transistion. Cu (II) complex shows peak at 230 nm which is attributed to $^{2}B1g \rightarrow {}^{2}Fg$ and $^{2}E1g \rightarrow {}^{2}A1g$ transitions and hence proves a octahedral configuration. Mn(II) shows a weak spin for forbidden transitions when compare to others. The electronic spectra it was concluded that all the metal complexes forms octahedral geometry. The electronic spectra was depicted in **Figure 10.3(a-j)**.

The **Figure 10.3(a'-j'),** the maximum level of the band absorption and band energies which were calculated using Tauc's equation.

$$(\alpha\hbar\upsilon)^{1/n} = A(\hbar\upsilon - Eg) \qquad \textbf{Eq.(10.1)}$$

According to the direct band-gap rule, $(\alpha\hbar\upsilon) = A(\hbar\upsilon - Eg)$ were plotted and then extrapolated to the X-axis. From the extrapolated curve, the band-gap energies for metal complexes were calculated from 3.2-4.8 eV respectively .

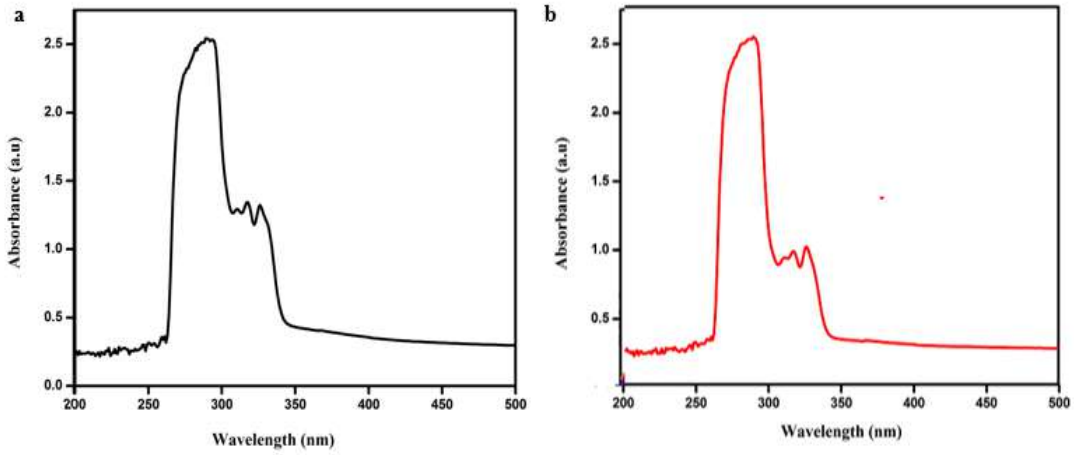

Figure 10.3 *UV-visible spectra of a) Mn (II) b) Co (II) complex*

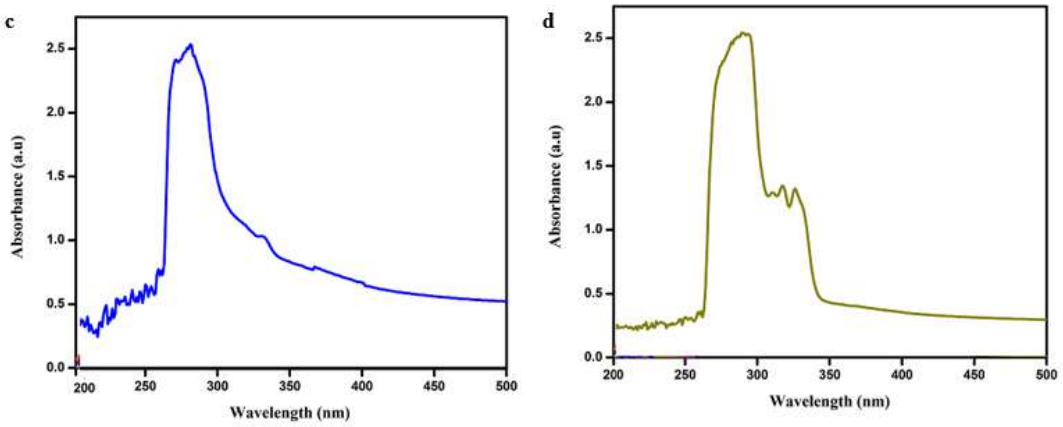

Figure 10.3 *UV-visible spectra of c) Ni (II) d) Cu (II) complex*

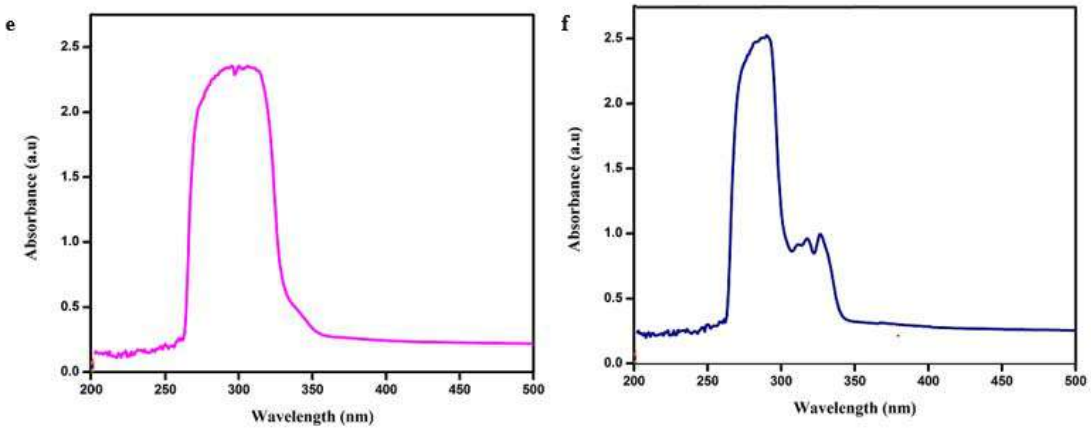

Figure 10.3 *UV-visible spectra of e) Zn (II) f) Cd (II) complex*

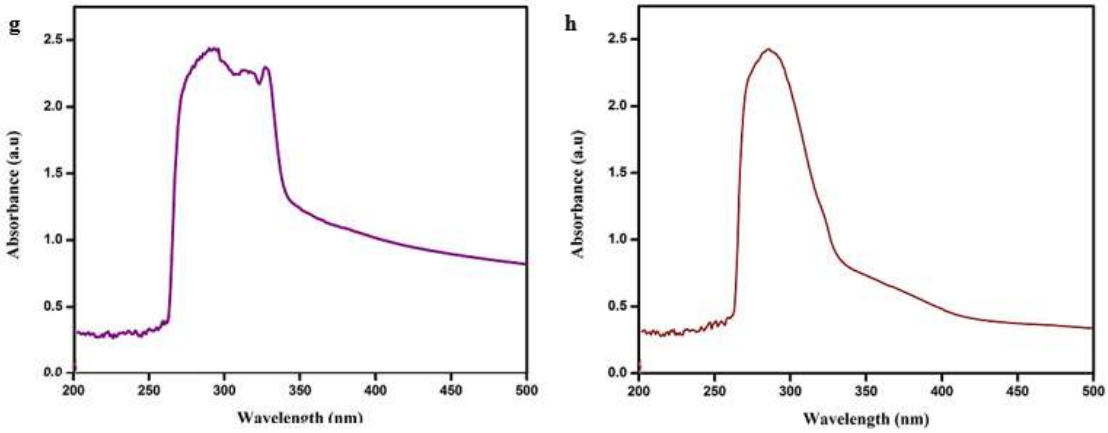

Figure 10.3 *UV-visible spectra of g) Ca (II) h) Sr (II) complex*

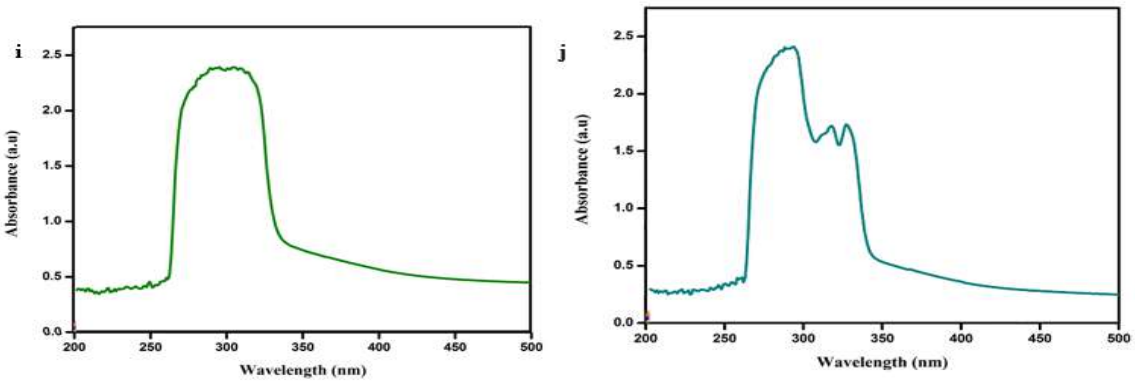

Figure 10.3 *UV-visible spectra of i) Ba (II) j) Mg (II) complex*

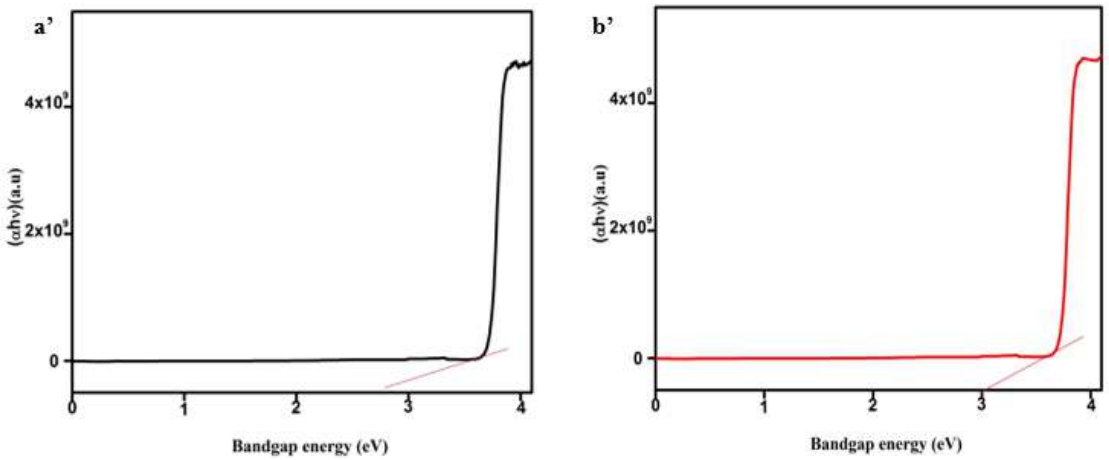

Figure 10.3 *UV-visible spectra of a') Mn (II) b') Co (II) complex*

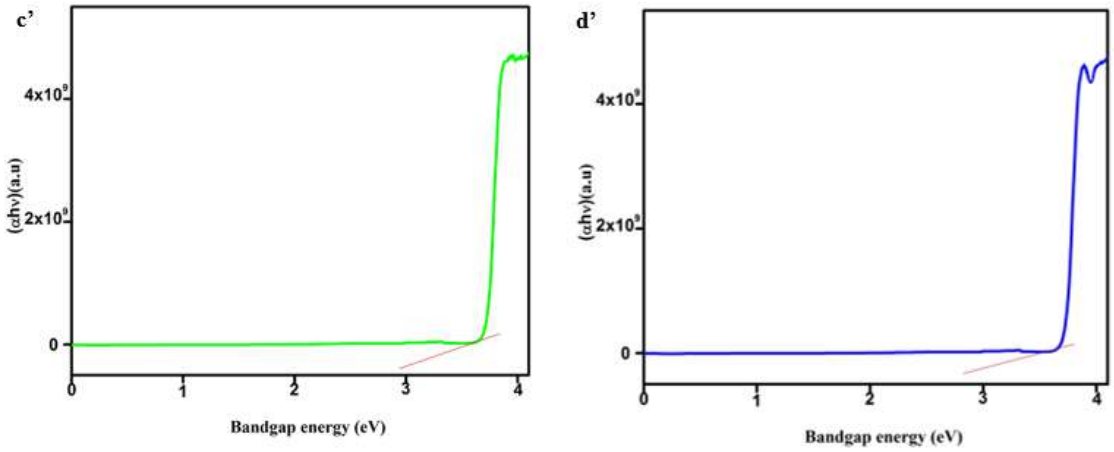

Figure 10.3 *UV-visible spectra of c') Ni (II) d') Cu (II) complex*

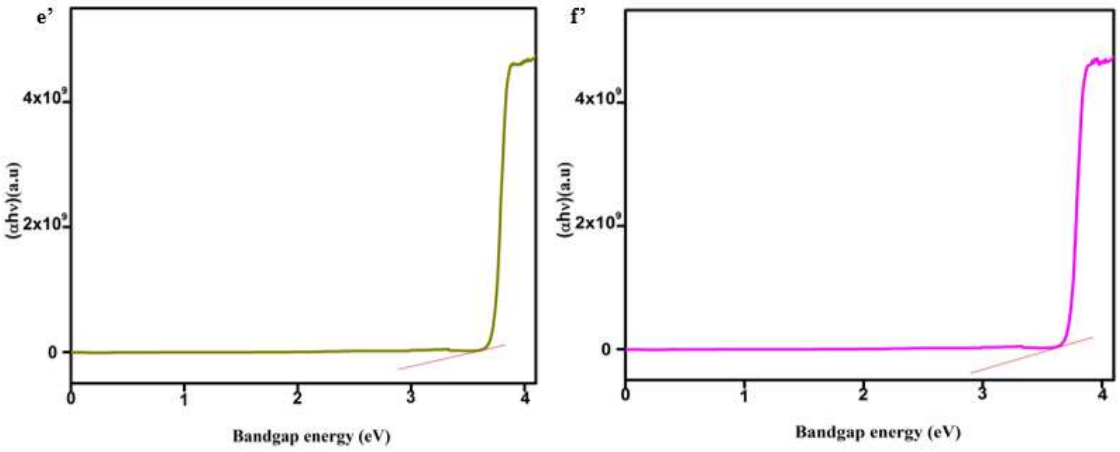

Figure 10.3 *UV-visible spectra of e') Zn (II) f') Cd (II) complex*

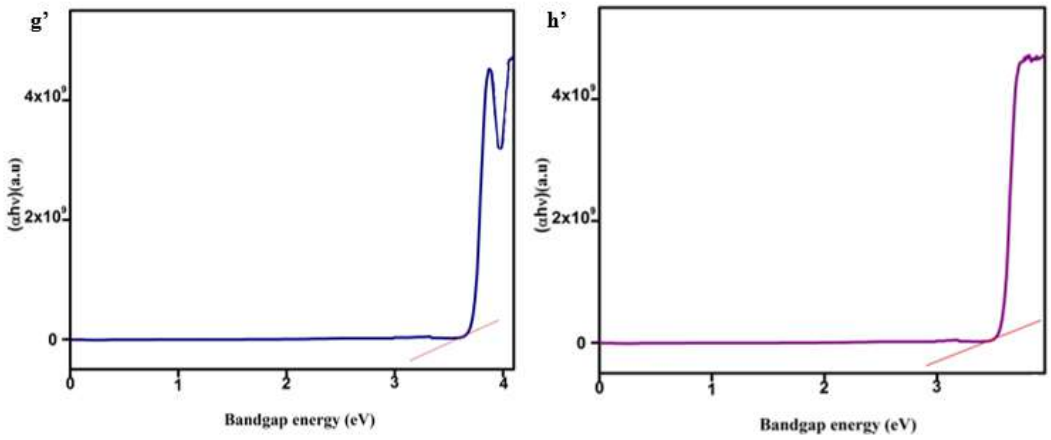

Figure 10.3 *UV-visible spectra of g') Ca (II) h') Sr (II) complex*

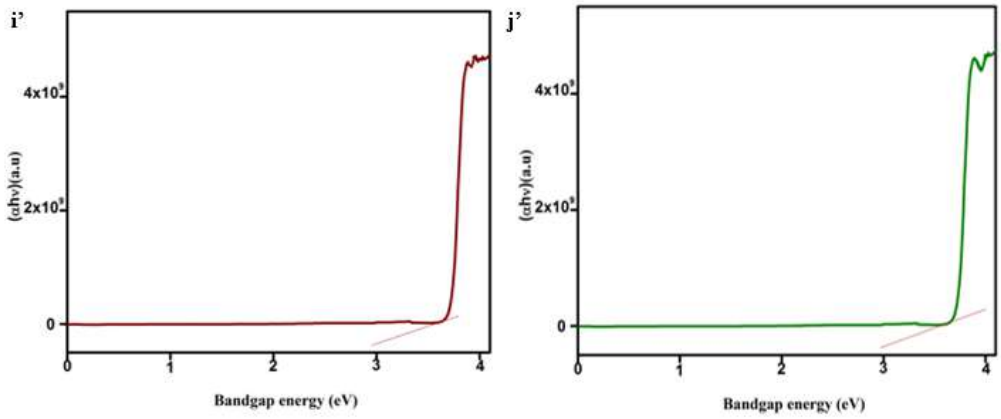

Figure 10.3 *UV-visible spectra of i') Ba (II) j') Mg (II) complex*

10.3.4 TG-DTA

TG-DTA of the metal complexes (**Figure 10.4**) is used to determine the presence of the volatile substance and the stability of the compound. Ni (II), Cu (II), Zn(II), and Ca (II) complexes shows mass loss in the temperature range, 190 °C -395 °C, followed by exothermic peak around 396°C, and finally metal oxide was obtained as final residue. For Mn (II), Co (II), Cd (II), Sr (II), Ba (II), and Mg (II) three-step decomposition process was obtained. Water molecules remove approximately at 200°C in the first phase the second phase is the removal of volatile organic compound and finally a metal oxide was formed, which is illustrated in **scheme (1)**.

Thermal decomposition scheme (1)

$[M(CH_5N_3)_2\ \{C_{10}H_7(2COO)\}_2.2H_2O] \xrightarrow{190\text{-}395\ ^0C} [M(CH_5N_3)_2\ \{C_{10}H_7(2COO)\}_2]\ -2H_2O$

$[M(CH_5N_3)_2\ \{C_{10}H_7(2COO)\}_2] \xrightarrow{396\text{-}400\ ^\circ C} [M\{C_{10}H_7(2COO)\}_2] - CH_5N_3$

$[M\{C_{10}H_7(2COO)\}_2] \xrightarrow{400\text{-}600\ ^\circ C} [MO]$

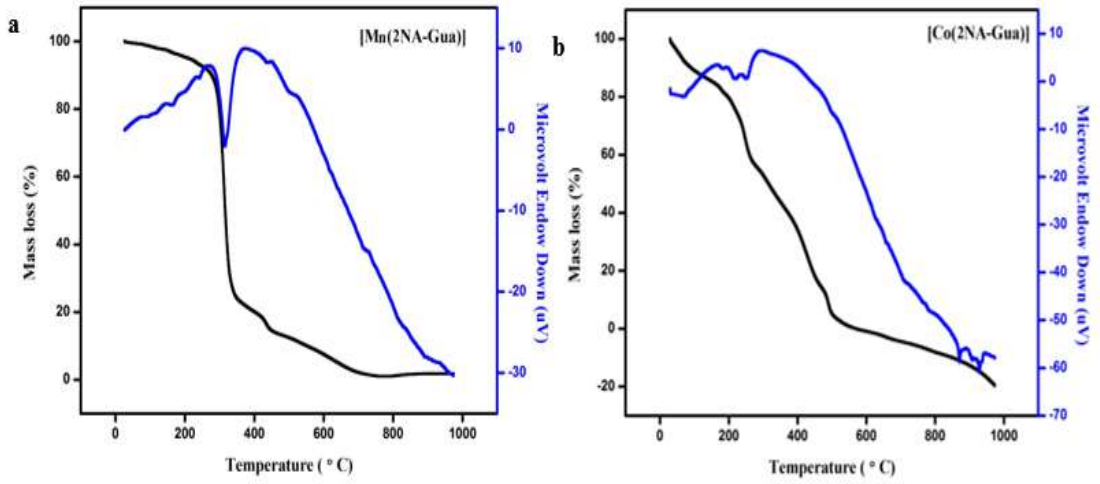

Figure 10.4 *TG-DTA a) Mn(II) b) Co(II) complex*

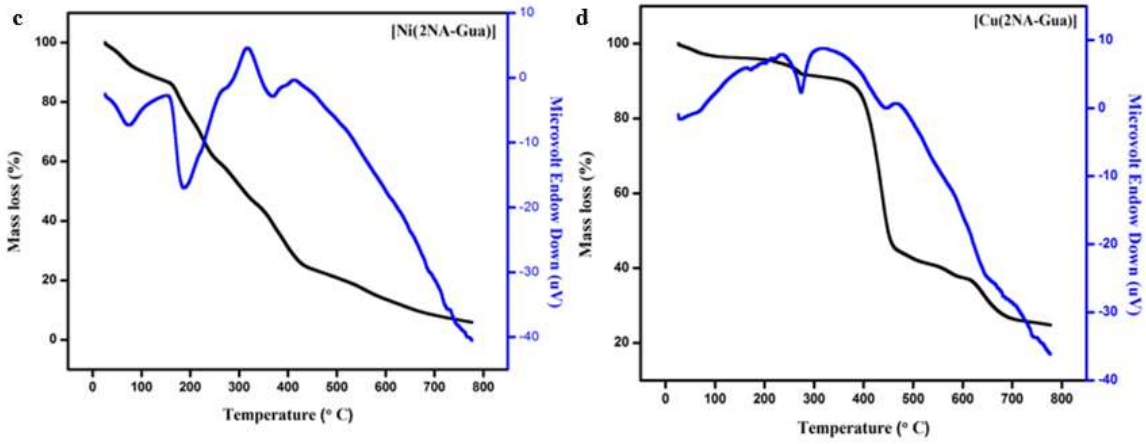

Figure 10.4 *TG-DTA c) Ni(II) d) Cu(II) complex*

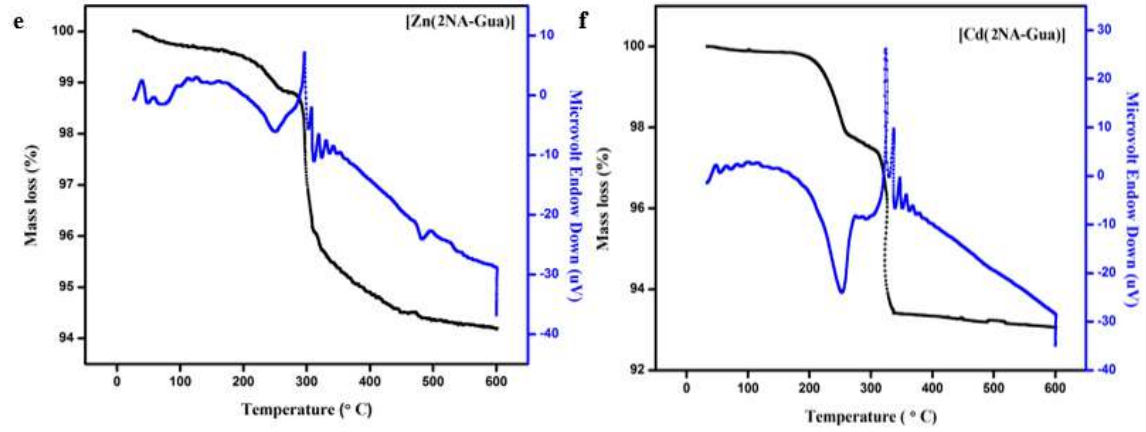

Figure 10.4 *TG-DTA e) Zn(II) f) Cd(II) complex*

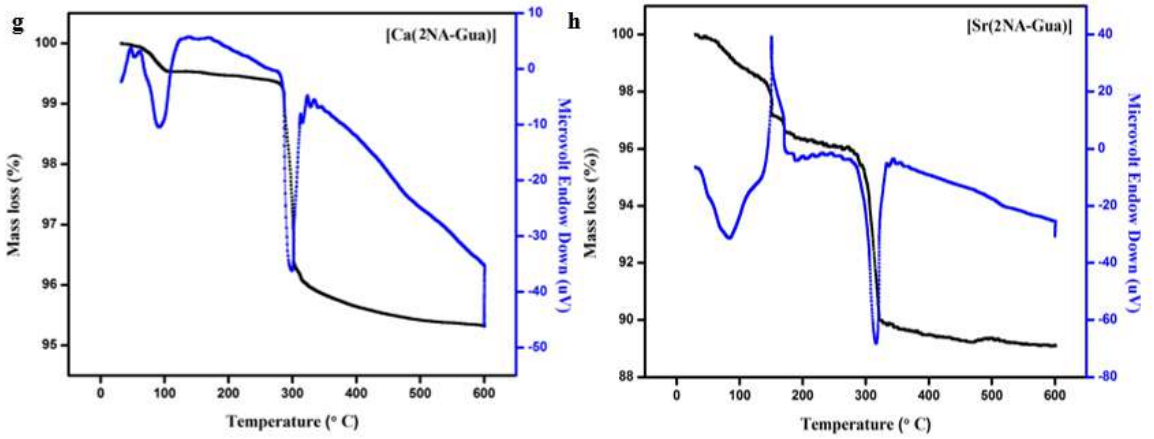

Figure 10.4 *TG-DTA g) Ca(II) h) Sr(II) complex*

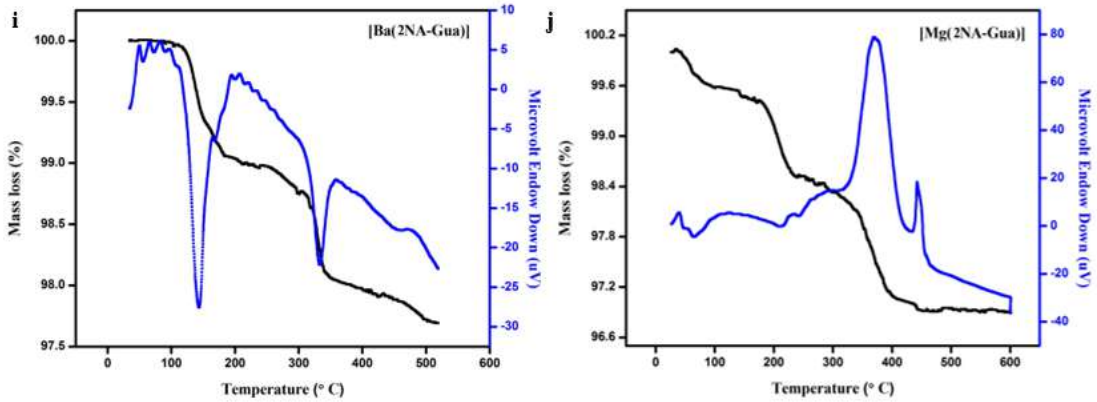

Figure 10.4 *TG-DTA i) Ba(II) j) Mg(II) complex*

10.3.5 Powder -XRD

The crystalline behaviour of the metal complexes was determined from XRD data. The hkl values and Miller indices were calculated from **Figure 10.5**. The crystallite size of the metal complexes was calculated from the Debye Scherrer equation, **Eq. (10.2)** and the particle size was found to be 29-36 nm respectively suggesting the complexes are in the nanocrystalline phase.

$$D = \frac{0.89\,\lambda}{\beta COS\theta} \qquad \textbf{Eq.(10.2)}$$

The d-spacing and the relative intensities of all the metal complexes was calculated and represented in **Table 10.5**.

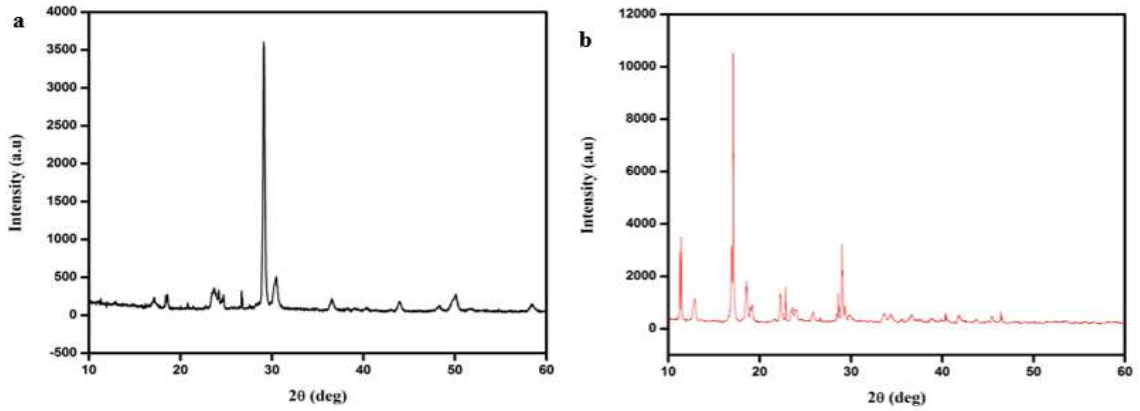

Figure 10.5 *Powder-XRD a) Mn(II) b) Co(II) complex*

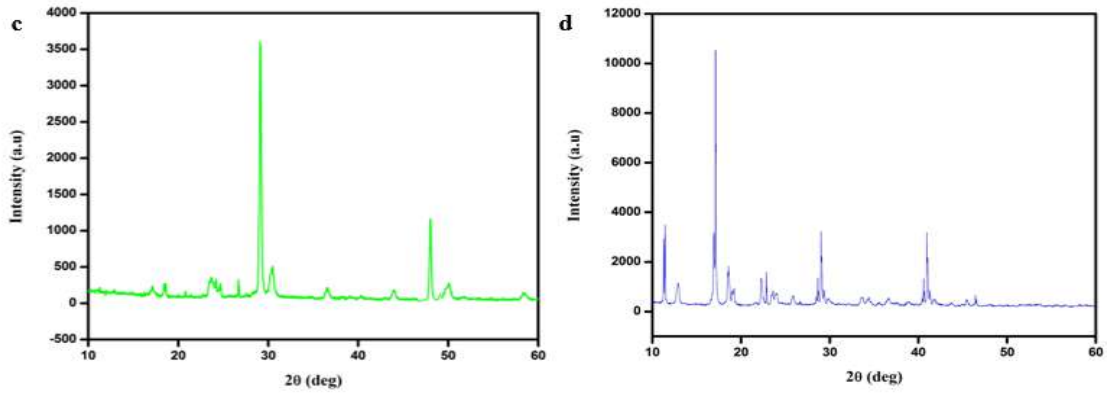

Figure 10.5 *Powder-XRD c) Ni(II) d) Cu(II) complex*

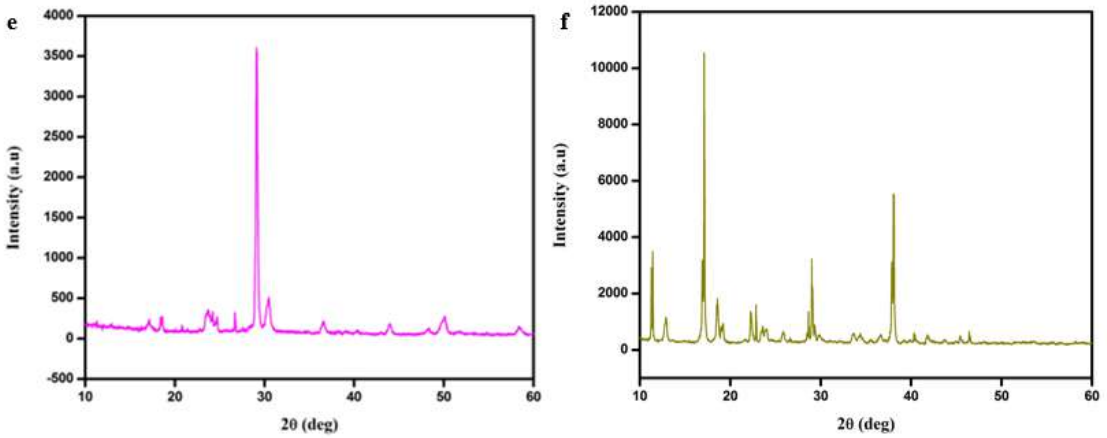

Figure 10.5 *Powder-XRD e) Zn(II) f) Cd(II) complex*

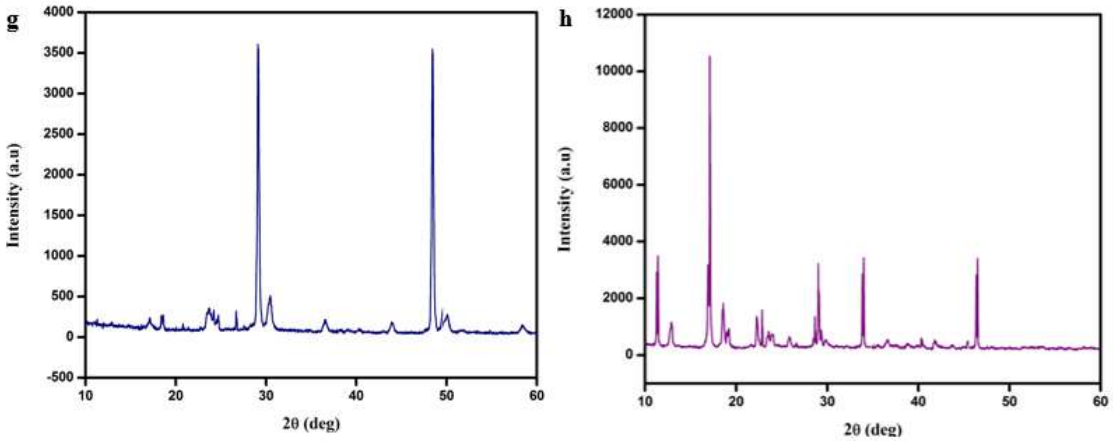

Figure 10.5 *Powder-XRD g) Ca(II) h) Sr(II) complex*

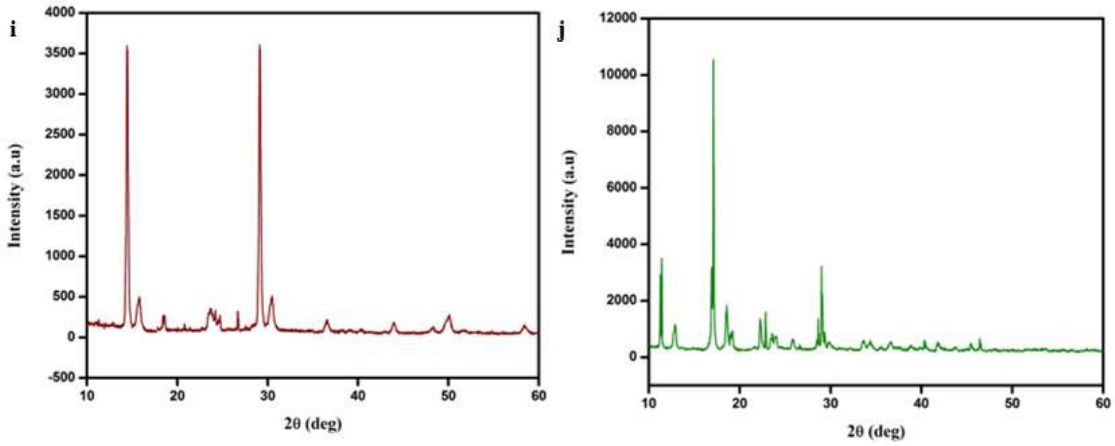

Figure 10.5 *Powder-XRD i) Ba(II) j) Mg(II) complex*

Table 10.5 *P-XRD pattern for metal complexes*							
Complex	**2θ**	**FWHM B_{size} (°)**	**D(space)**	**Complex**	**2θ**	**FWHM B_{size} (°)**	**D(space)**
$[Mn(C_2H_8N_4O_3)_2\{C_{10}H_7(2COO)\}_2.2H_2O]$	16.1	0.461	18.19	**$[Cd(CH_5N_3)_2\ C_{10}H_7(2COO)\}_2.2H_2O]$**	12.2	0.461	18.11
	19.4	0.469	17.96		16.21	0.469	17.88
	21.4	0.463	18.25		18.99	0.463	18.18
	27.2	0.502	17.02		24.76	0.502	16.94
	29.5	0.565	15.20		26.4	0.565	15.10
$[Co(C_2H_8N_4O_3)_2\{C_{10}H_7(2COO)\}_2.2H_2O]$	13.8	0.461	18.14	**$[Ca(CH_5N_3)_2\ C_{10}H_7(2COO)\}_2.2H_2O]$**	12.5	0.461	18.12
	19.0	0.469	17.95		16.5	0.469	17.89
	22.4	0.463	18.29		19.4	0.463	18.20
	27.7	0.502	17.04		25.0	0.502	16.94
	31.0	0.565	15.25		26.4	0.565	15.10
$[Ni(C_2H_8N_4O_3)_2\{C_{10}H_7(2COO)\}_2.2H_2O]$	12.6	0.461	18.12	**$[Sr(CH_5N_3)_2\ C_{10}H_7(2COO)\}_2.2H_2O]$**	12.5	0.461	18.12
	16.4	0.469	17.89		16.1	0.469	17.88
	18.8	0.463	18.18		19.2	0.463	18.19
	23.2	0.502	16.89		24.7	0.502	16.94
	26.5	0.565	15.10		26.7	0.565	15.11
$[Cu(C_2H_8N_4O_3)_2\{C_{10}H_7(2COO)\}_2.2H_2O]$	12.0	0.461	18.11	**$[Ba(CH_5N_3)_2\ C_{10}H_7(2COO)\}_2.2H_2O]$**	12.5	0.461	18.12
	16.0	0.469	17.88		16.1	0.469	17.88
	19.0	0.463	18.19		19.2	0.463	18.19
	21.8	0.502	16.85		24.7	0.502	16.94
	27.0	0.565	15.12		26.7	0.565	15.11
$[Zn(C_2H_8N_4O_3)_2\{C_{10}H_7(2COO)\}_2.2H_2O]$	12.5	0.461	18.12	**$[Mg(CH_5N_3)_2\{C_{10}H_7(2COO)\}_2.2H_2O]$**	12.82	0.461	18.13
	16.1	0.469	17.88		16.1	0.469	17.88
	19.2	0.463	18.19		18.88	0.463	18.18
	23.4	0.502	16.89		24.86	0.502	16.94
	26.6	0.565	15.10		26.71	0.565	15.11

10.3.6 Antimicrobial activity towards metal complexes

The results of the antibacterial analysis of the corresponding metal complex Ni (II), Co (II), Cu (II), and Zn (II) are summarized in **Table 10.6**. The synthesized compounds generally showed antibacterial activity for all microbes, except Zn (II) complexes exhibited exceptional potential against *E. coli*, and *Staphylococcus aureus* with inhibition zones in the ranges of 13.2,and 11.9 mm . The antibacterial activities of complexes may be attributed to the involvement of hyper-conjugation and induction of greater lipo solubility. The polarity of metal ions diminished and caused delocalization of π-electrons, which, in turn, favored the penetration of complexes through the bacterial membrane, subsequently enhancing their activity which is shown in **Figure10.6,** and **10.8 a**.The antifungal activities against *Aspergillus fumigates* shows moderate inhibitory growth zones. The Zn (II) inhibits the fungal strains and resulted in inhibitory zones of 10.3 mm in diameter as shown in **Table 10.7.** However, Zn (II) ions were adsorbed to a greater extent onto the surface of fungal cell walls when compared to other metal ions in which they were illustrated in **Figure 10.7,**and **10.8b.**

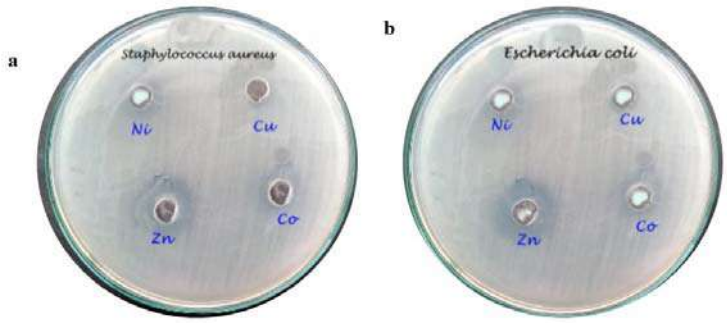

Figure 10.6 *Antimicrobial activity of Zn (II) complex against a) Staphylococcus aureus b) Escherichia coli*

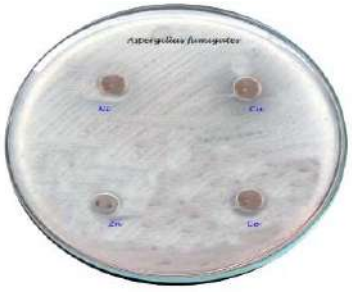

Figure 10.7 *Antifungal activity of Zn (II) complex against Aspergillus fumigates*

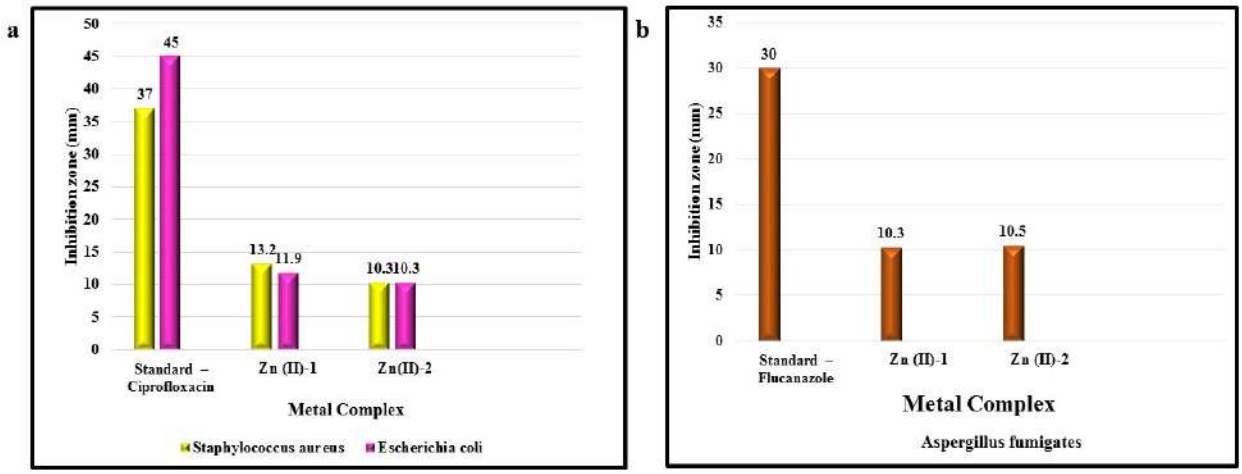

Figure 10.8 *Inhibition evaluation of the Zn (II) complex against a) Bacteria b) Fungal*

Table 10.6 *Antibacterial activity*		
Compound	***Inhibition zone (mm) (100µg/disc)***	
	Staphylococcus aureus	***Escherichia coli***
Standard – Ciprofloxacin	37	45
Zn(II)-1	11.9	13.2
Zn (II)-2	10.3	10.3

Table 10.7 *Antifungal activity*	
Compound	***Inhibition zone (mm) (100µg/disc) Aspergillus fumigates***
Standard – Flucanazole	30
Zn(II)-1	10.5
Zn (II)-2	10.3

10.3.7 Anti-Oxidant activity

The antioxidant activity of Zn (II) is estimated by using the scavenging of the DPPH (2, 2′ -diphenyl-1-picryl hydroxyl) radical. The scavenging measurements of DPPH• were determined spectrophotometrically. DPPH was prepared in methanol, and 1 ml of DPPH methanol solution was mixed with different concentrations of 30, 60, 90, 120, 150 µg/ml. The reaction was set aside in the dark for 30 min. The reduction of DPPH• was observed by a decrease in absorbance with solvent and DPPH as blank. The percentage inhibition of DPPH activity was calculated using the following method.

$$Inhibition\ of\ DPPH\ activity\ (\%) = \frac{A_{control} - A_{sample}}{A_{control}} X\ 100 \qquad \textbf{Eq.(10.3)}$$

Where $A_{control}$ = absorbance of DPPH• in methanol without an antioxidant,

A_{sample} = absorbance of DPPH• in the presence of an antioxidant

Table 10.8. illustrates the antioxidant activity of the compound. From the experimental outcomes, enhanced antioxidant activity is detected at concentration 150, which shows good inhibition **(Figure 10.9)** Among all the metal complexes, Zn (II) shows more antioxidant activity.

Table 10.8 *Antioxidant Activity*

Concentration (µg/ml)	**% Inhibition**
30	65.65
60	77.14
90	83.25
120	92.01
150	94.2

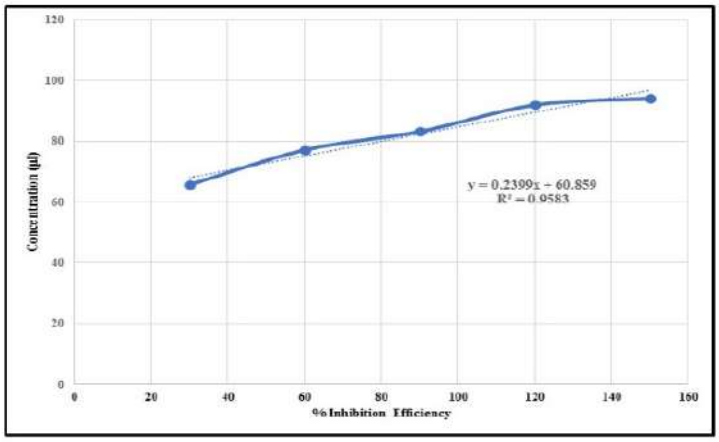

Figure 10.9 *Inhibition efficient plot of antioxidant activity*

10.4 APPLICATION ON ORGANIC LIGHT-EMITTING DIODES USING METAL COMPLEXES

10.4.1 Photoluminescence spectra

10.4.1.1 Photoluminescence spectra of Ni (II) complex

Emission spectra of the Ni (II) complex show excitation at 389 nm and two robust, broad bands at 343, 66 and 778 nm. The d^8 system of Ni^{2+} ions can occur octahedral geometry. But the attained energy levels are allocated to distorted octahedral geometry and assigned as $A_{2g}(F) \rightarrow T_{2g}(F)$, $A_{2g}(F) \rightarrow T_{1g}(F)$ & $A_{2g}(F) \rightarrow T_{1g}(P)$. In addition, spin-allowed transitions (2) and spin-forbidden transitions (1) were observed. The luminescence properties of Ni (II) exist in two segments, namely green and red, which are designated to the $T_{2g}(D) \rightarrow A_{2g}(F)$ & $T_{2g}(D) \rightarrow T_{2g}(F)$ transitions.

10.4.1.2 Photoluminescence spectra of Co (II) complex

The band of cobalt emission occurs around 600–700 nm, allocated to $^2E(2G) \rightarrow {}^4A_2(4F)$ of the octahedral environment. The Co (II) complex displays an excitation peak at 370 nm associated with three strong, broad bands at 343 nm, 626 nm & 778 nm. The existing peak confirms the bivalency state of cobalt ions in an octahedral environment. For Co^{2+} ions in the ground state, 4F splits into $^4T_1$, $^4T_2$, and $^4A_2$ states, with the $^4T_1$ state being the lowest one.

In addition to that, it exhibits two emission bands in the visible region, which were assigned to $^4T_1(4P) \rightarrow {}^4A_2(4F)$ and ^{4T1} (4P) $\rightarrow {}^4T_2(4F)$ octahedral. Compared with other complexes, the cobalt moiety shows enhanced emission spectra, which may be recognized in the MLCT process (metal-to-ligand charge transfer). It offers excellent coordination abilities for complex [2].

10.4.1.3 Photoluminescence spectra of Cu (II) complex

For the Cu (II) complex, emission spectra show an excited peak at 433 nm with three strong emission bands ranging from 433 to 800 nm; the primary emission peak is detected at 454 nm and the other at 626 nm & 778 nm. In agreement with crystal field theory, the d^9 Cu^{2+} ion splits into E_g and T_{2g}, with E_g being the ground state.

The Photoluminescence spectra for all metal complexes are revealed in **Figure 10.10a**. The diffuse reflectance spectra of synthesized compounds powder samples were collected to measure the optical band gap energy (E_g). The optical band gap energy was evaluated as the connection point between the energy axis and the extrapolated line from the straight line of the absorption edge in a plot of Kubelkas Munk function vs. energy. The band gap values for emission spectra are observed at 2.01 eV, 2.86 eV, and 2.87 eV, respectively, as shown in **Figure 10.10 b**. The emission spectra inferred that the photoluminescence was directly associated with band gap energy. The band structure illustration as attained through the DFT scaffold is shown in **Figure 10.10c**.

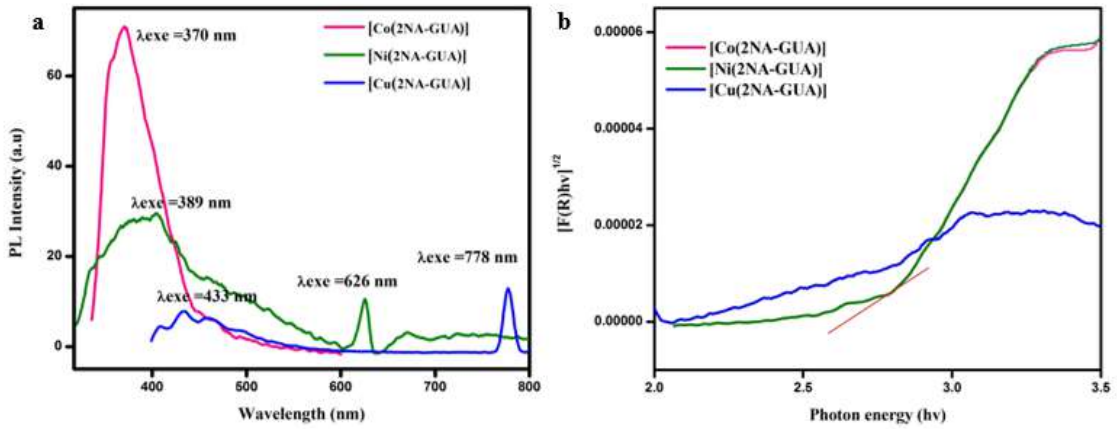

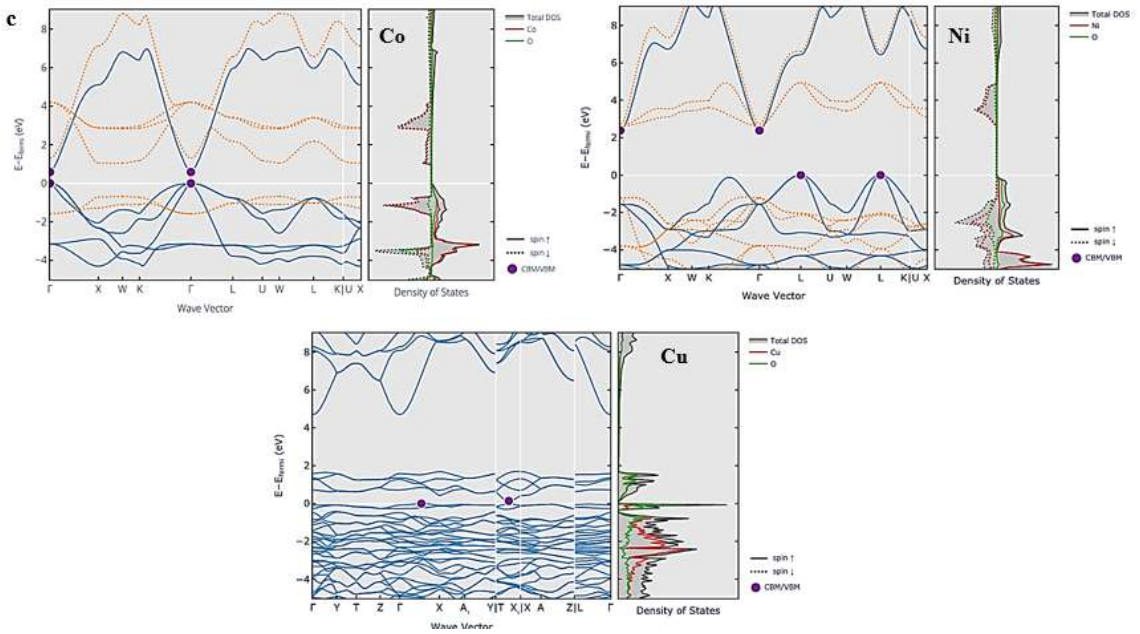

Figure 10.10 *a) Photoluminescence of metal complexes b) Band gap c) Band structure from the DFT framework*

10.4.1.4 Jablonski Energy Level

Jablonski represents the energy level within a molecule where the valency electron can be excited. The absorption of a photon from a particular energy level in the molecule results in the migration of electrons from the lower energy, ground state S_0 state, to the higher energy, excitation state S_1, which is indicated by the violet arrow in **Figure 10.11**. The light green arrow lying between the electronic states represents the migration of electrons that lose their absorbed energy from the higher energy state to the lower energy state by emitting photons. The fluorescence process occurs from 10^{-9} to 10^{-7} seconds, most frequently between the first excitation electron state and the ground state. The electronic state of F in the ground is represented by A_{2g} +T_{1g} +T_{2g}, D indicates E_g + T_{2g}, and P represents T_{1g}.

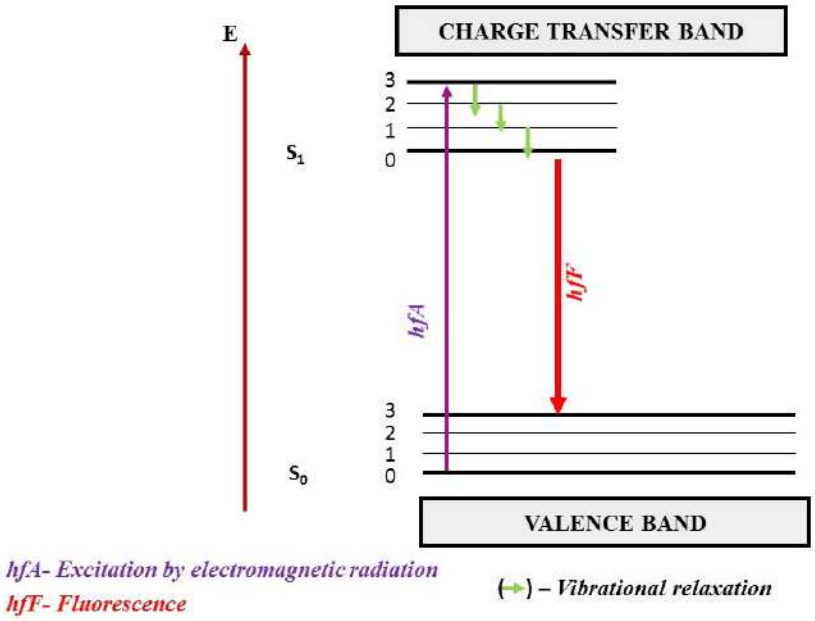

Figure 10.11 *Proposed Jablonski diagram*

10.4.2 Decay lifetime curve

Luminescence decay curves were attained at room temperature by scrutinizing all transition states of the metal complexes (626 nm) and they are represented in **Figure 10.12**. The PL decay curves show good fit with only one exponential and for (Ni(2NA-GUA)) at $A_{2g}(F)$ — $T_{2g}(F)$, (Co(2NA- GUA))at $T_1(4P)$ - $A_2(4F)$ and (Cu(2NA- GUA)) displays 3d $4s^1$- $3d^{10}$ triplet transitions in the discharge(emission) spectrum. After 500 nm, the intensity of the peak was low- ered, which may be due to concentration quenching-transfer of energy from radiative to non-radiative ions. The decay lifetime was found to be 441 µs, 530 µs and 450 µs respectively, as shown in **Table 10.9** and results infer that all complexes have a good promising luminescence character for light- emitting diode applications [3].

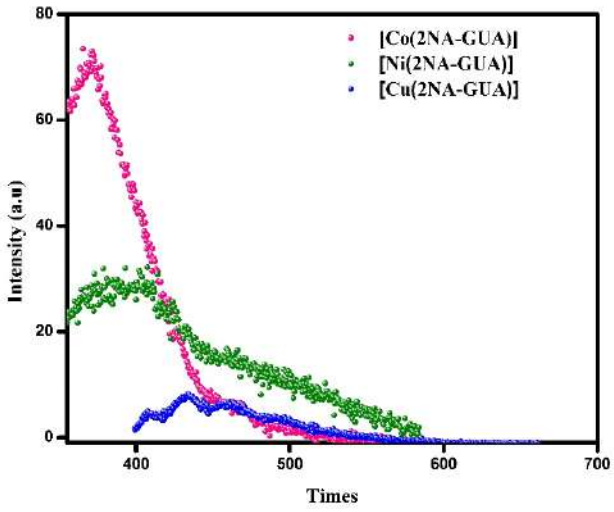

Figure 10.12 *PL decay spectrum for metal complexes*

Table 10.9 *Interpretation of photoluminescence metal complexes decay*			
Metal complexes	τ_1	τ_2	R^2
[Co(2NA-GUA)]	409	445	0.969
[Ni(2NA-GUA)]	373	446	0.912
[Cu(2NA-GUA)]	456	510	0.762

10.4.3 Chromaticity Coordinate (CIE) and color purity

The fundamental physical property of all light sources is the spectral power of light at all wavelengths. Chromaticity coordinates are evaluated from the spectral power distribution (SPD) and plotted as a two-dimensional graph to deliver the color communication of the given light source. Each color represents the suitable and distinctive diagram's point, whose positional variables are parallel to chromaticity coordinates. The CIE 1931 chromaticity X, Y coordinates (x, y) are evaluated from luminescence emission spectral data with the help of color-matching methods. The color of the light discharged from the source is denoted by the (x, y) coordinate revealed on a chromaticity diagram **(Figure 10.13)**. From this diagram, one can illustrate the influence of ions on the color of the emitted light. The line is stretched from white to blue, and the coordinates (color) position is denoted by a solid circle in the CIE diagram. CIE chromaticity

coordinates of the test molecules and their values are presented in **Figure 10.13b** and **Table 10.10**. The observed CIE values range from X= 0.26 to 0.14, Y= 0.26 to 0.14. These results clearly showed the luminescence properties of synthesized complexes and had great hope as a blue phosphor in OLED applications. It is evident from the values that the Cu ion emits in the blue region, and a digital photograph is placed inside **Figure 10.13a,** which also reveals blue emission.[4,5]

The purity of the color was derived from the below equation

$$\%CP = \frac{\sqrt{(X-X_i)^2+(Y-Y_i)^2}}{\sqrt{(X_d-X_i)^2+(Y_d-Y_i)^2}}\ X\ 100 \qquad \textbf{Eq.(10.4)}$$

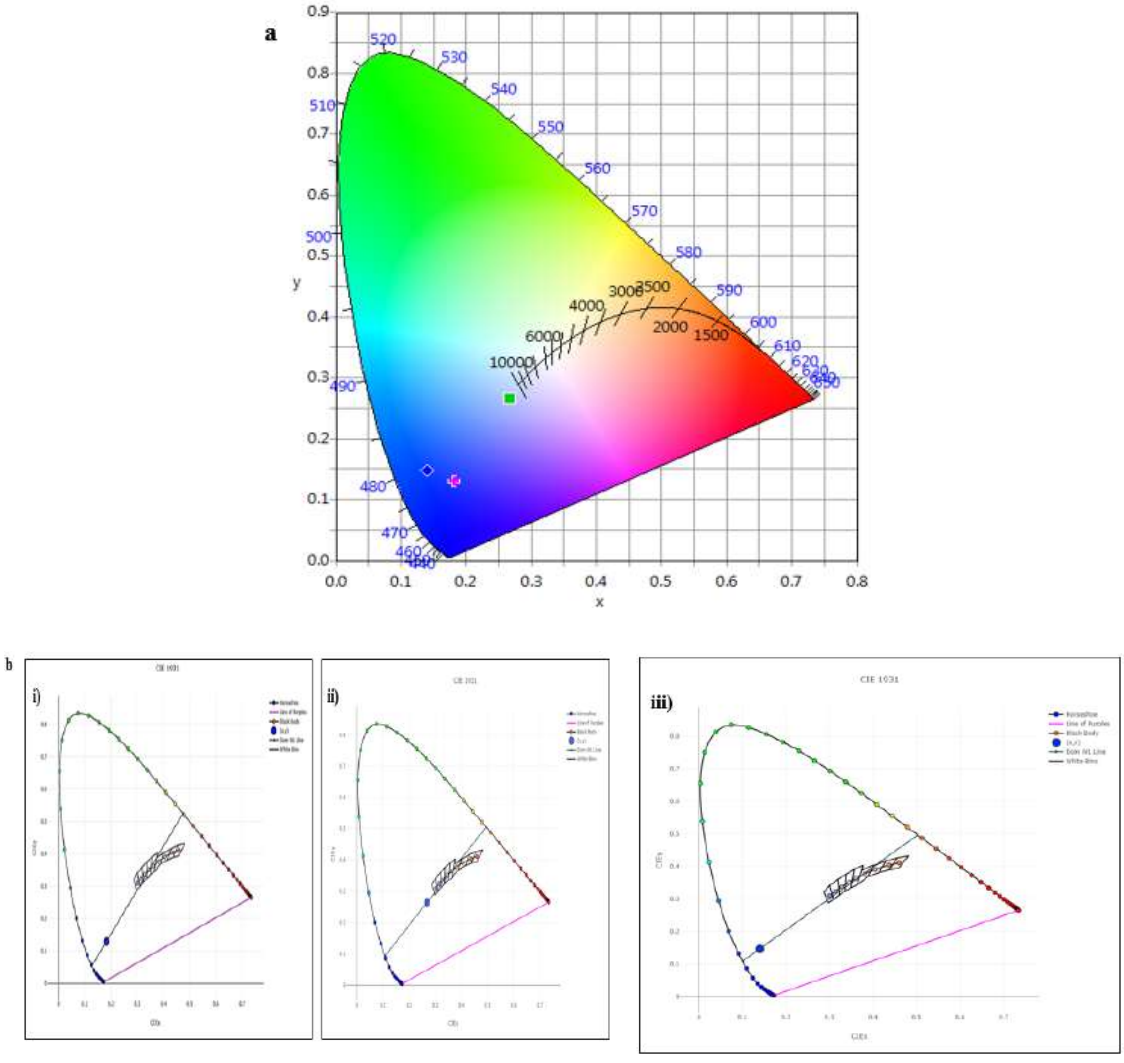

Figure 10.13 *a) CIE chromaticity coordinates b) Dom Wavelength i) [Co(2NA-GUA)], ii)[Ni(2NA-GUA)] and iii)[Cu(2NA-GUA)]*

Table 10.10 *CIE Chromaticity Coordinate, Dom wavelength, and Color purity*			
Sample Code	**CIE Chromaticity**	**Dom Wavelength (nm)**	**Color Purity (%)**
[Co(2NA-GUA)]	(0.1829, 0.1295)	469	72.8
[Ni(2NA-GUA)]	(0.2684, 0.2648)	476	28.6
[Cu(2NA-GUA)]	(0.1404, 0.1473)	478	82.8

10.4.4 Correlated Color Temperature (CCT) and Duv values

The CCT and Duv values are shown in **Table 10.11**. The value of CCT was observed from the chromaticity using Mc Camy's formula.[6]

$$CCT_{test} = -449n^3 + 3525\,n^2 - 6838\,n + 5520.33 \qquad \textbf{Eq.(10.5)}$$

The CCT value determined the brightness and the visual recognition by the sources which are indicated by 'warm' or 'cool'. Delta u, v signifies the light distance from the black body curve which is represented by the 'pure white' light sources. Duv is represented by ANSI C78.377 the recommended value should lie between ± 0.006. The negative -Duv value shows the color point from beneath the black body curve and is presented in the maroon or pink portion and the +Duv value shows the point over the black body curve and is represented in the green or yellow color portion.[7] The metal complex's Duv values occur around (-0.0049 to -0.175) which represents the negative Duv value which is closely related to the white light emission (**Figure 10.14)**.

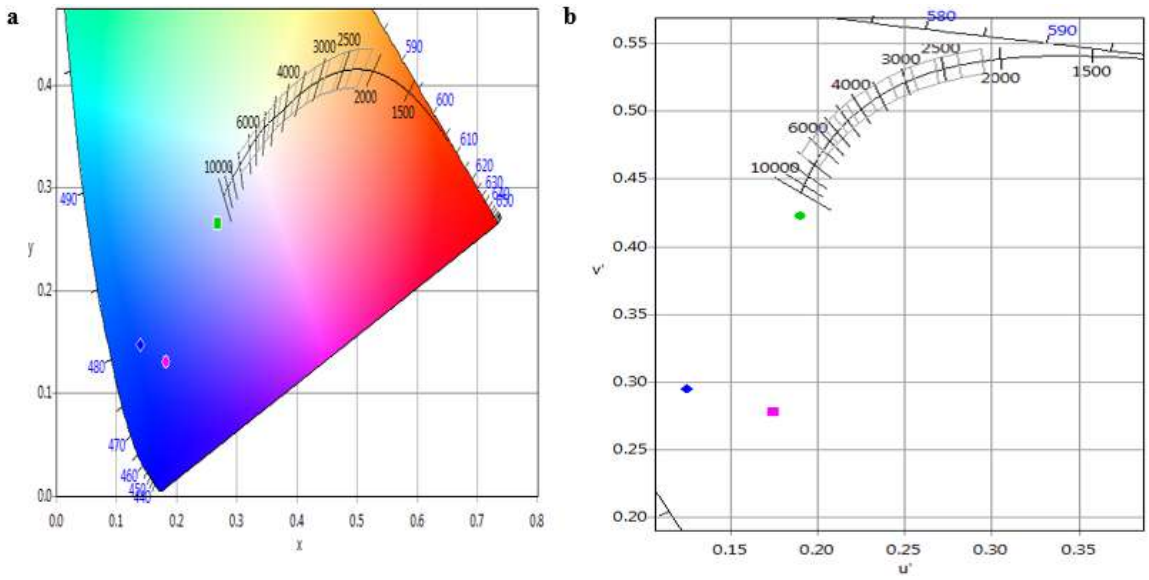

Figure 10.14 *a)Correlated Color Temperature was determined using Planckian locus b) color consistency and its stability was evaluated using Δu'v'*

Table 10.11 *Duv metric is evaluated with the help of CIE 1931*							
Sample Code	**CCT (K)**	**X**	**Y**	**U'**	**V'**	**Duv**	**Du'v'**
[Co(2NA-GUA)]	4486	0.1829	0.1295	0.1747	0.2783	-0.0784	-0.1175
[Ni(2NA-GUA)]	13602	0.2684	0.2648	0.1903	0.4225	-0.0046	-0.0049
[Cu(2NA-GUA)]	6695	0.1404	0.1473	0.1252	0.2955	-0.0865	-0.1143

10.4.5 Color Rendition Index

Color rendering index (CRI), referred to as the CIE test color method, was used to differentiate the color rendering effect of a new light source compared with the traditional one. CRI is an important grade for fluorescent tubes since they are missing portions of the spectrum and talk about the difference's magnitude. The light sources with similar CRI values will render different colors.

The primary metric of the CIE is Ra which was determined from the average value of the first eight colors and typically ranges from 0 to 100; even negative values are possible. For the nickel complex (**Figure 10.15**), Ra = 72.12, which means that it can be used for workplace lighting and high-quality light applications, but for cobalt (II) and copper (II) complexes, negative values are obtained. In addition, for nickel (II) complex, %CRI is 95, confirming the earlier statement (**Table 10.12**) [8] .

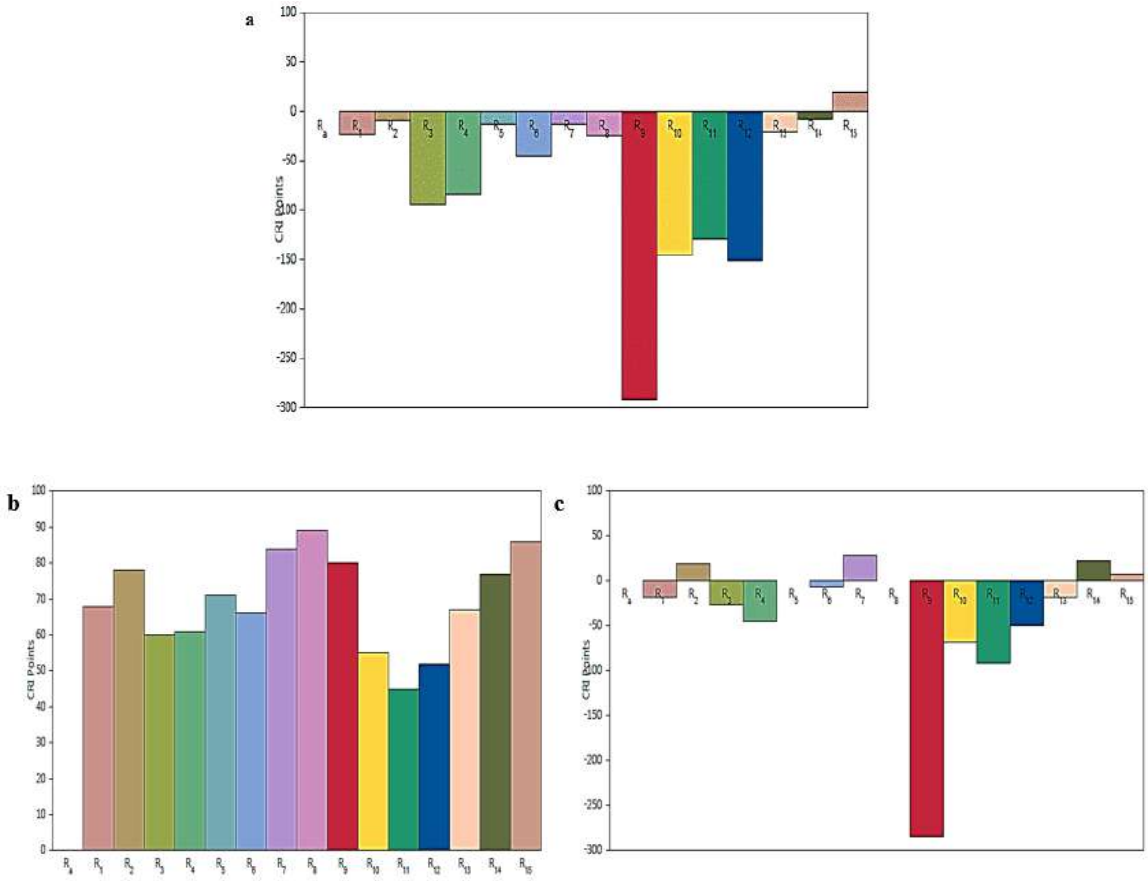

Figure 10.15 *Color Rendition Metrics i) [Co(2NA-GUA)], ii)[Ni(2NA-GUA)] and iii)[Cu(2NA-GUA)]*

Table 10.12 *Color rendering index (CRI) measured from R1 to R15 of the optimal WLED lamp*															
Samples	R1	R2	R3	R4	R5	R6	R7	R8	R9	R10	R11	R12	R13	R14	R15
[Co(2NA-GUA)]	-24	-10	-95	-84	-13	-46	-13	-25	-292	-146	-130	-152	-21	-9	20
[Ni(2NA-GUA)]	68	78	60	61	71	66	84	89	80	55	45	52	67	77	86
[Cu(2NA-GUA)]	-19	19	-27	-46	0	-8	28	0	-286	-69	-92	-50	-19	23	8

10.4.6 TLCI (Television Lighting Consistency Index)

The European Broadcasting Union 3355 has established a novel model called Television Lighting Consistency Index TLCI-2012. It is used to evaluate the color rendering of a light source produced on television, or camera. It is compared with CRI, the only necessity for TLCI is spectral power distribution. This TLCI software compares with the spectral data from the ideal sources which are useful in television production. There is a 24 rating color in which occurs maximum value produces 100. The rating color values depend upon the color value level in TLCI shown in **Figure 10.16**. Ni (II) complexes show the TLCI=100 which specifies the light source is widely observed for television uses as for the Co (II)and Cu (II) the TLCI=1 in which color produce bad and they are not applicable in the broadcast.[9]

The Society of Motion Picture and Television Engineers (SMPTE) color blocks were updated in software to promote the setting display color and their color controls. In which TLCI-2012 in the figure shows the warm diode and the left end which is represented by V-WHITE in which the chip emits the monochromatic light approximately equal to 405 nm represented by violet light instead of blue light chips in which common white light is used as an emitter which range occurs from 450-460 nm.[9]

From the **Figure 10.16** top right table is the colorist advice report in which zero shows the perfect color version if a single + or – symbol indicates the error is very minor

if it is multiple signs it represents that there is a need for a higher magnitude improvement. This statement was compared with the Co (II), Ni (II), and Cu (II) in which Ni (II) complexes show the zero value this makes a perfect color version when compared with the other two metal complexes. [9]

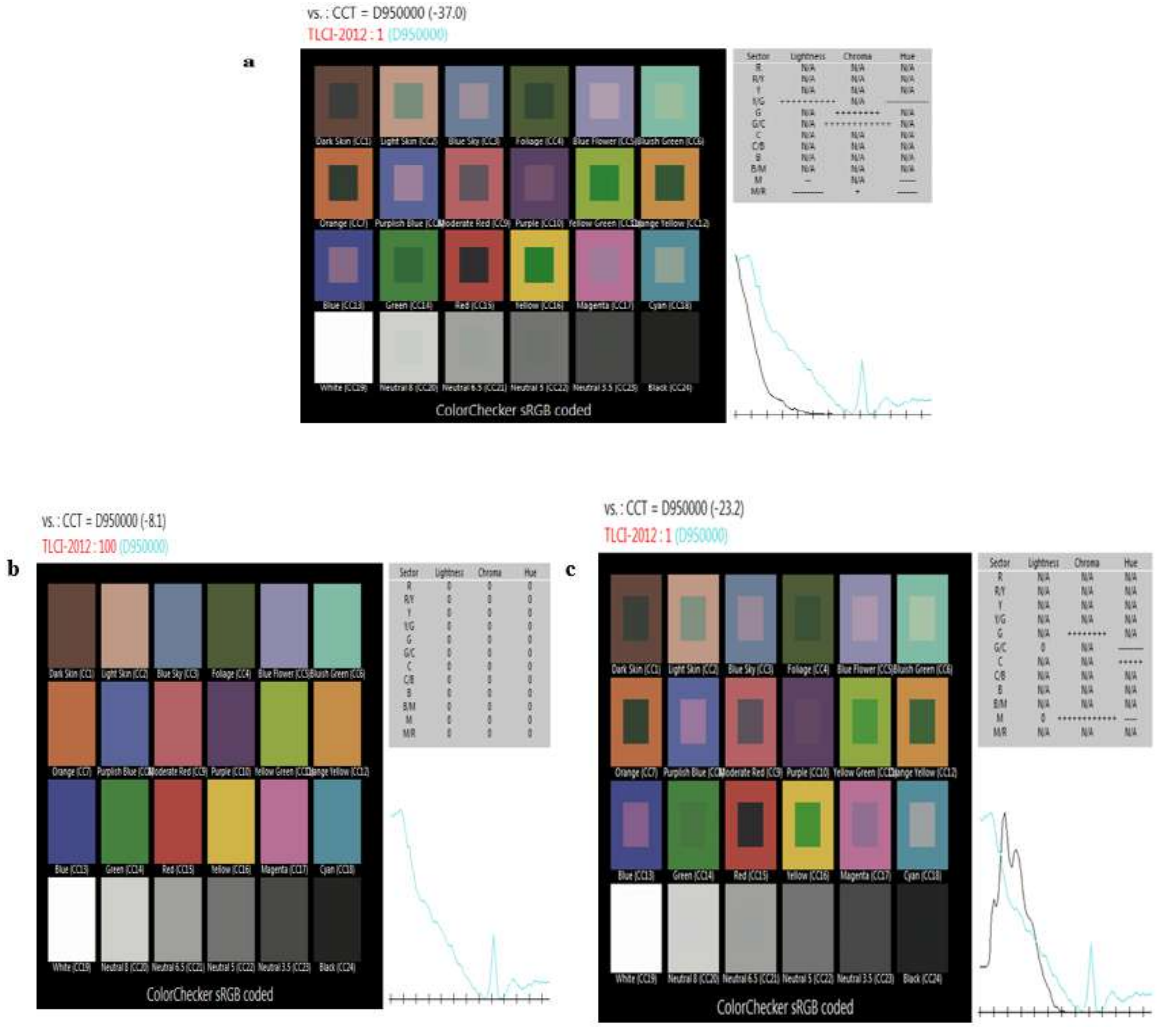

Figure 10.16 *Television Lighting Consistency Index for a) Co (II) b) Ni (II) and c) Cu (II) metal complexes*

*10.4.7 CIE L*a*b* Coordinates*

From **Figure 10.17** CIE L*a*b* is used to identify the numeric color shades and their color spaces which were taken from the two measurements values from the digitized images attained in the form of photographic. The L*, a*, and b* signify the three values in

the color space that is used to measure the object-specific color and the calculated color differences from the image. In which

L*= denotes the lightness

a*= red/ green coordination

b*= blue/yellow coordination and

ΔL*, Δa*, and Δb* in which delta produces the positive or negative sign. The over total delta (ΔE*) value always produces the positive which is illustrated in **Table 10.13**. It is understood they are considered in commercial production, but their color variance occurs as perceived by printing and graphic professionals. [10]

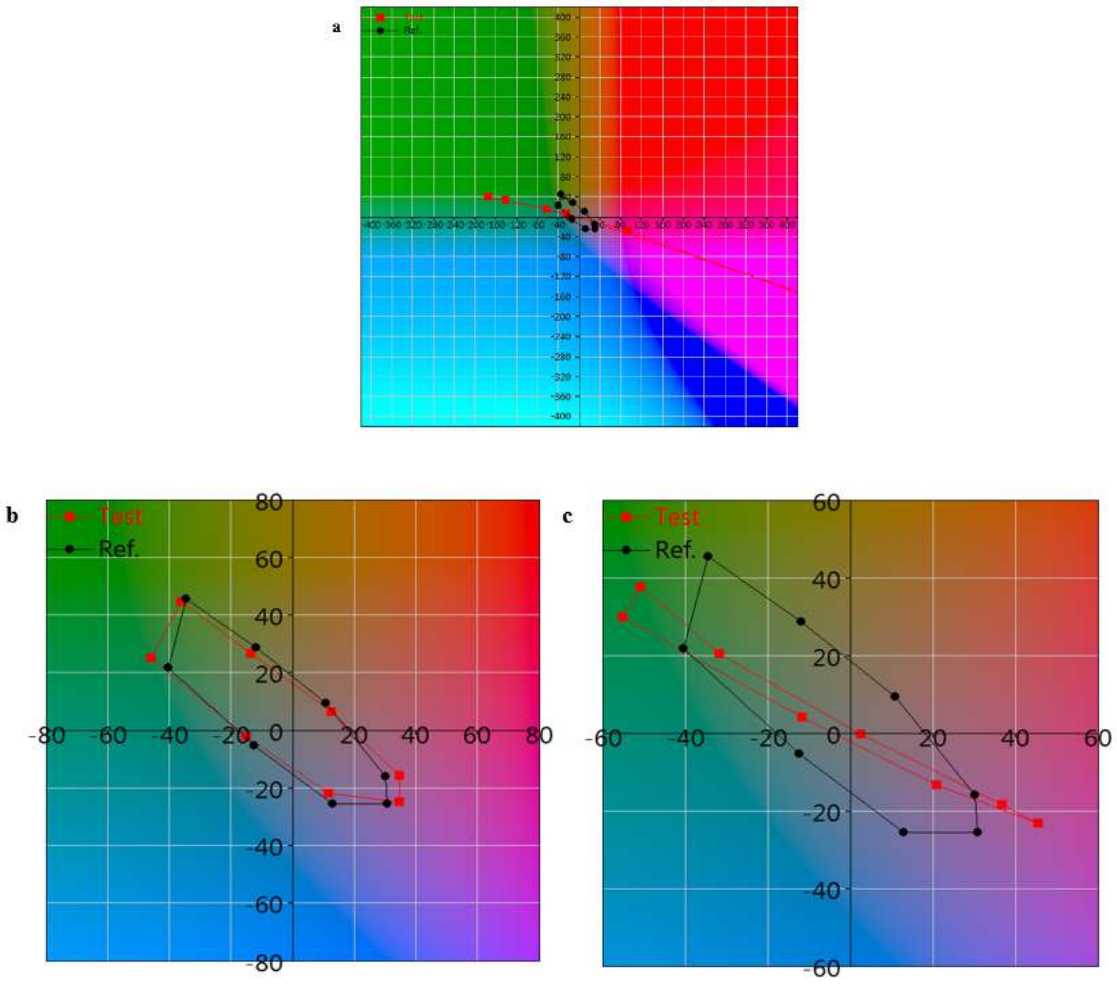

Figure 10.17 *CIE L*a*b* Coordinates a) Co (II) b) Ni (II) and c) Cu (II) metal complexes*

Table 10.13 *CIE of ΔL*, Δa* and Δb* and (ΔE*)*				
Sample	**ΔL***	**Δa***	**Δb***	ΔE*
[Co(2NA-GUA)]	-1675.2	7228.3	-2865.0	9228.3
[Ni(2NA-GUA)]	3.91	-11.9	10.02	69.79
[Cu(2NA-GUA)]	-16.63	-165.26	-27.08	313.2

10.4.8 Test Colour Sample (TCS)

Figure 10.18 shows the test color sample which is used to describe the color precision and fidelity. The TCS is used to calculate 8 color samples and additional 7 supplementary colors in the CRI metric [11].

The Score is represented by R_i, which illustrates the TCS number. Which R_i used to evaluate the 15 samples, is based on human vision (Ra). For example, TCS09 refers to a deep red color it indicates the color quality for several applications [12].

The test color samples described in the CRI metric are shown below

Test Code	***Colour of the Sample***	***Test Code***	***Colour of the Sample***
TCS01	Light grayish red	TCS08	Light reddish purple
TCS02	Dark grayish-yellow	TCS09	Strong red
TCS03	Strong yellow-green	TCS10	Strong yellow
TCS04	Moderate-yellowish green	TCS11	Strong green
TCS05	Light bluish green	TCS12	Strong blue
TCS06	Light blue	TCS13	Light yellowish pink
TCS07	Light violet	TCS14	Moderate olive green
TSC15 Olive Hue			

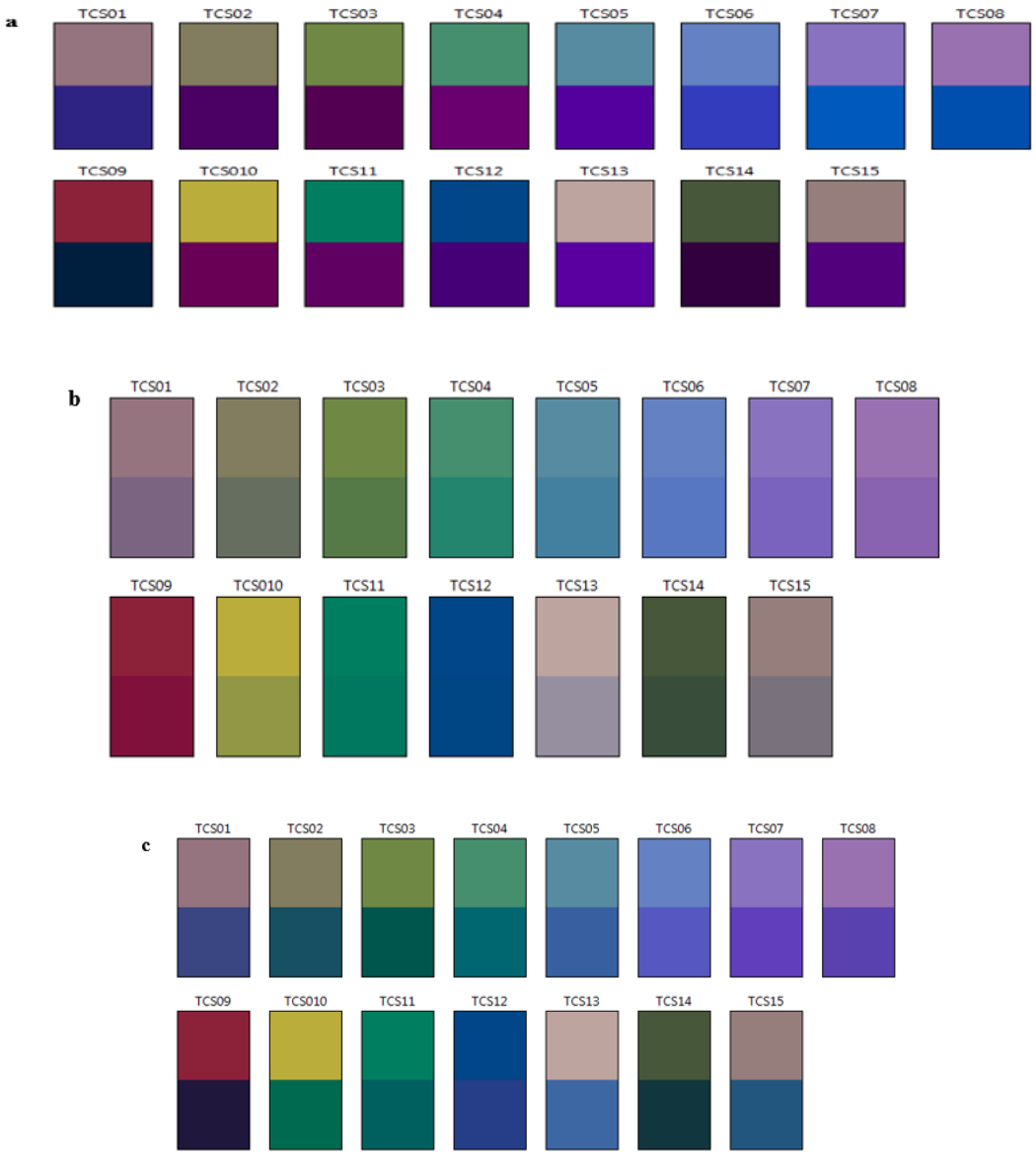

Figure 10.18 *Test Colour Sample (TCS) a) Co (II) b) Ni (II) c) Cu (II) complex*

10.5 APPLICATION ON EPOXY RESIN-BASED $CeMnO_3$, CeO_2, and Mn_3O_4 OXIDE NANOCOMPOSITE

10.5.1 Vibrational Spectra

The FTIR spectral analysis of the composite metal oxide (**Figure 10.19**) sample exhibits that the M-O linkage was observed around 462 cm^{-1} to 505 cm^{-1}, and it is clear that the spectra of $CeMnO_3$ are entirely different from CeO_2, and Mn_3O_4, which proves the presence of two metal ions [13–16].

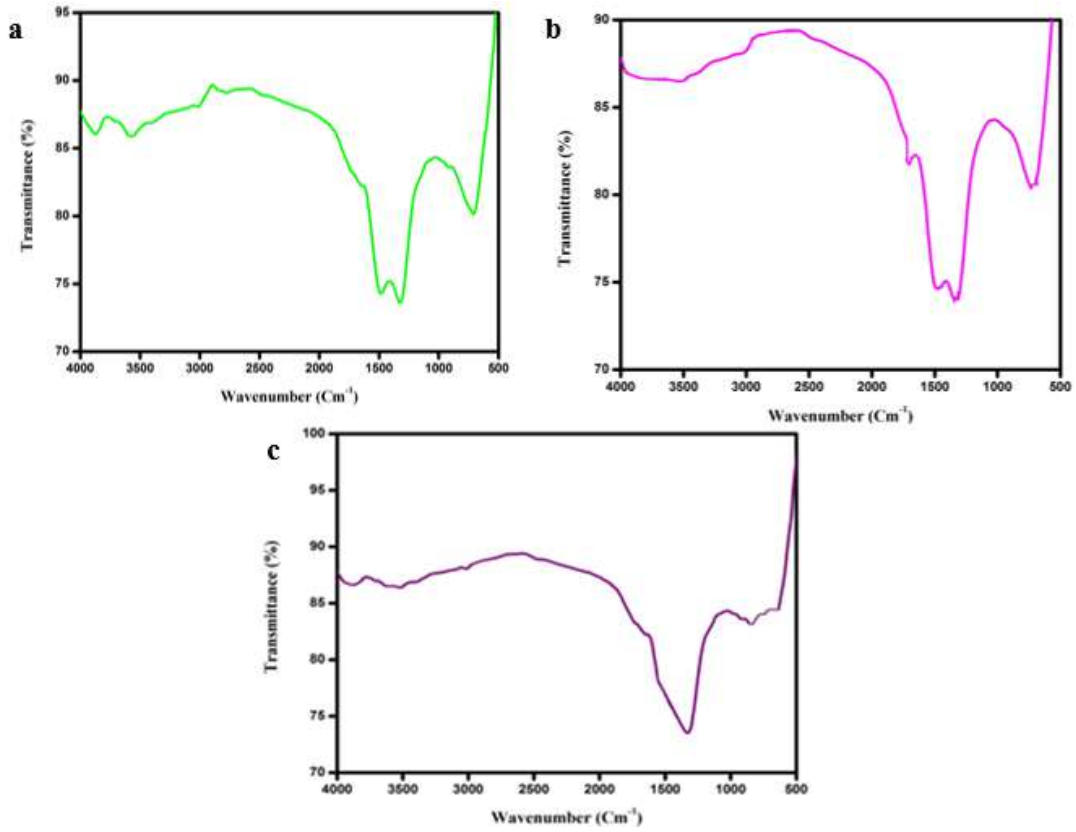

Figure 10.19 *FT-IR of metal oxide a) $CeMnO_3$ b)* CeO_2, *and c)* Mn_3O_4

10.5.1.1 Electronic Spectra

At room temperature, absorption spectrum of the prepared metal oxide in the DMSO was determined and shown in **Figure 10.20**. The composite metal oxide absorption bands were observed at 231 nm for CeO_2 and 327 nm for Mn_3O_4 and 250,360 nm for CeMnO.

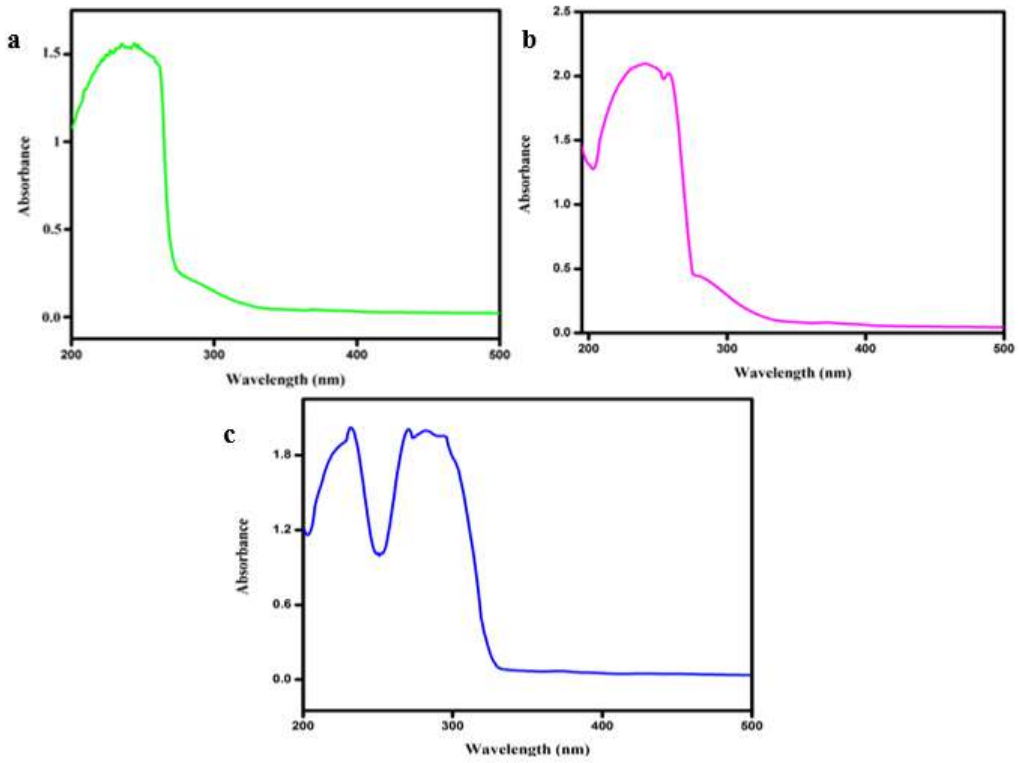

Figure 10.20 *UV-visible spectra of metal oxide a) CeO_2, b) Mn_3O_4 and c) $CeMnO_3$*

10.5.1.2 TG-DTA of metal oxide

Figure 10.21 represents the thermogram of the complex with a very slight endotherm peak at 120℃, owing to the removal of water molecules in the complex. The exothermic peak from 346℃ to 495℃ is due to the disintegration of acid and the ligand moiety and leads to the formation of metal oxide. The composite metal compound undergoes various decomposition steps, and the proposed degradation pattern is shown below in **Scheme (2)** .

Thermal decomposition scheme (2)

$$Ce(CN_3H_5)_2\{C_{10}H_7(COO)\}.H_2O \xrightarrow{100-292℃} [Ce(CN_3H_5)_2\{C_{10}H_7(COO)\}]$$

$$[Ce(CN_3H_5)_2\{C_{10}H_7(COO)\}] \xrightarrow{292-390℃} [Ce\{C_{10}H_7(COO)\}]$$

$$[Ce\{C_{10}H_7(COO)\}] \xrightarrow{390-518℃} [CeO_2]$$

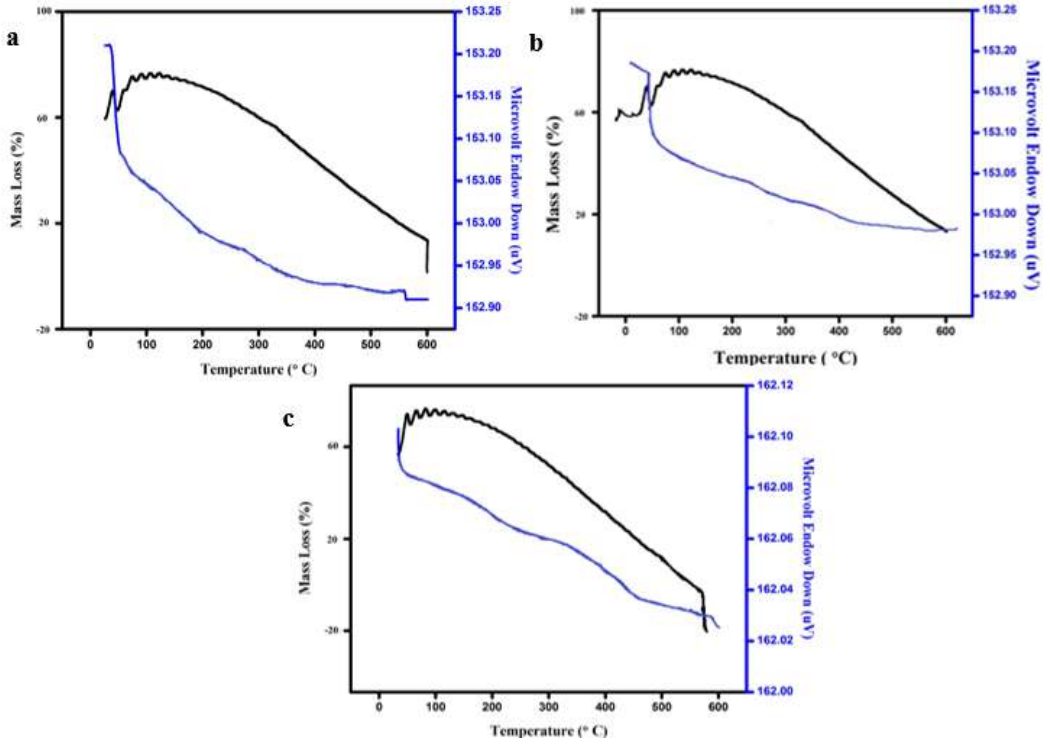

Figure 10.21 *TGDTA of metal oxide a) CeO_2, b) Mn_3O_4 and c) $CeMnO_3$*

10.5.1.3 Powder- XRD of metal oxide

Powder-XRD intense peaks can be seen in the (**Figure 10.22)** of $CeMnO_3$, indicating the purity of the sample. The obtained value of 2θ was confirmed with the Joint Committee on Powder Diffraction Standards (JCPDS) with the card number 34-0394 for $CeMnO_3$. In the case of $CeMnO_3$, the diffraction peaks shift to higher 2θ. The four main diffraction peaks of $CeMnO_3$ are assigned to the (111), (022), (022), and (220) planes, and for the MnO the JCPDS is 78-0420.In hich it confirms the metal oxide and represented the intense peaks in the XRD pattern, which indicated oxide was highly pure [17].

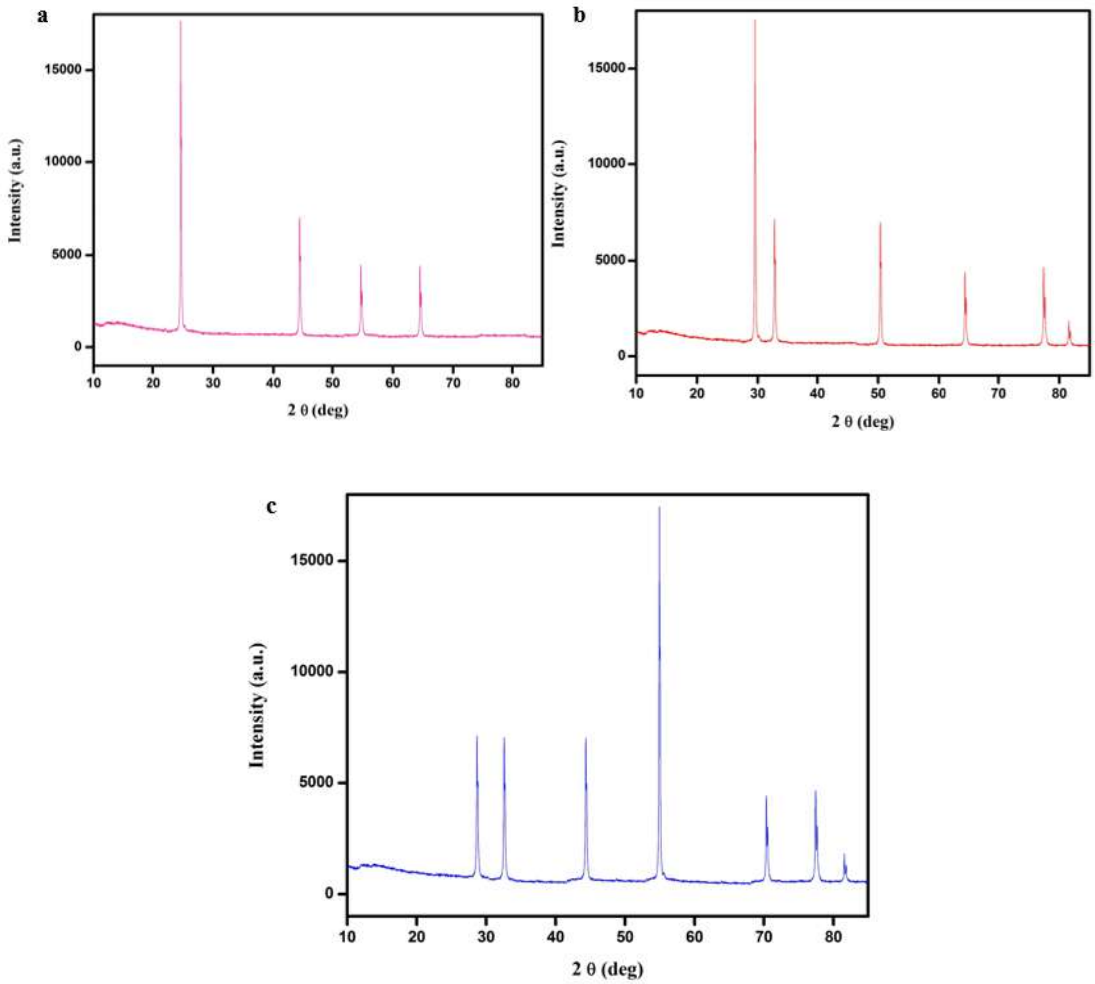

Figure 10.21 *Powder XRD patterns of metal oxide a) CeO_2, b) Mn_3O_4 and c) $CeMnO_3$*

10.5.1.4 Morphology of metal oxide

SEM images of nano metal oxides, which confirm that they have a homogenous size with a spherical shape. It is worth mentioning that the amount of Ce^{2+} ion adsorbed will be higher than Mn^{2+} ions (32% Ce and 27% Mn) as displayed in energy dispersive X-ray analysis **(Figure 10.23 a-c)**). The HR-TEM examination **(Figure 10.23 d)** with the inset of the average size distribution curve discloses that composite metal oxide has a cubic assembly with a shell-like structure [18,19].

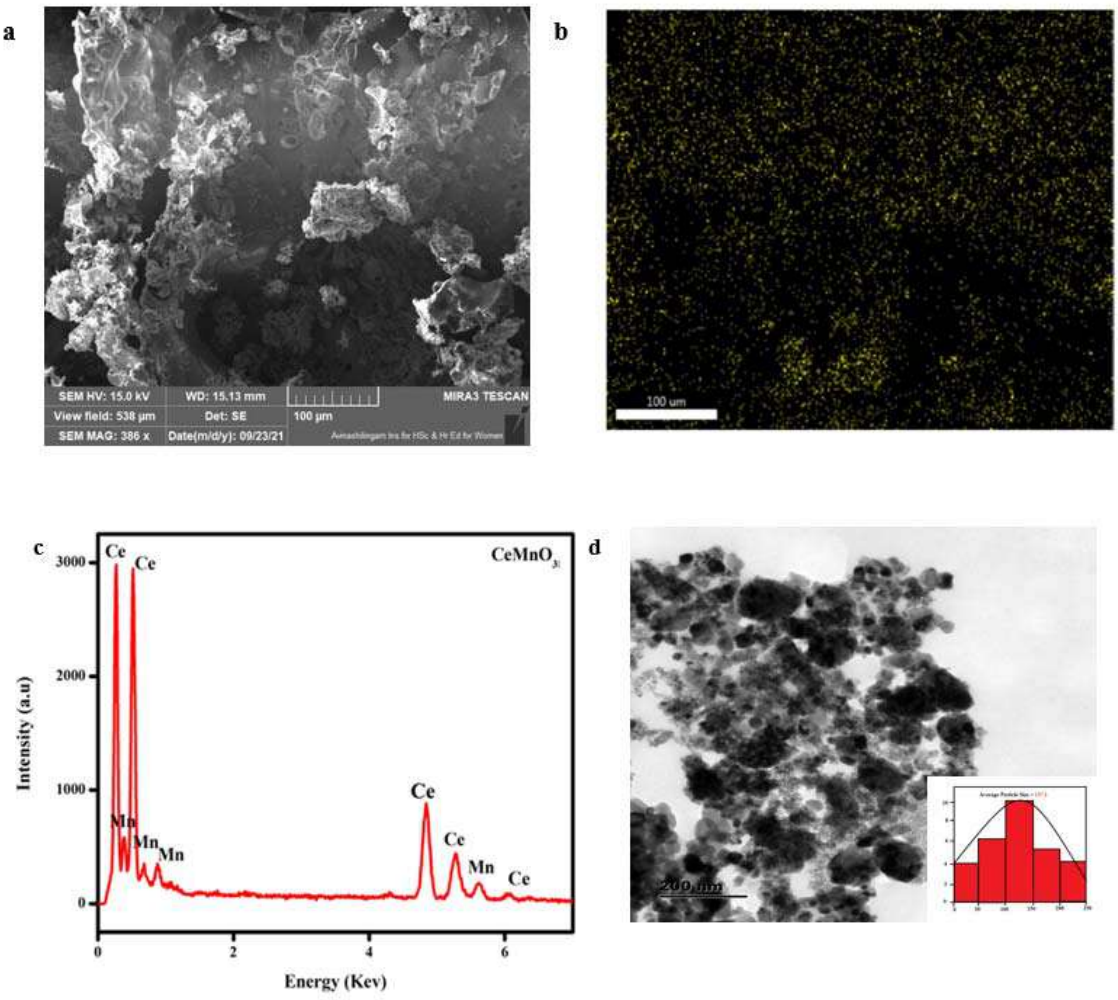

Figure 10.23 *$CeMnO_3$ a) SEM images, b) Colour mapping c) EDX analysis and d) TEM and HR-TEM analysis.*

10.5.2 Salt-spray corrosion

The inhibition activity of the $CeMnO_3$, CeO_2, and Mn_3O_4 exposed to salt fog from 24 hours to 120 days was examined, and the photographs are shown in **Figure 10.24 (a-c)**. All the plates show flat surfaces without much corrosion effect. Compared to other coatings, cerium oxide-coated plates are prone to corrosion due to higher cationic charges. The composite metal oxide coating was stable up to 120 days. The rust of the salt fog on the metal surface is due to electrochemical reaction in which the oxidation layer containing the chloride ions protects the layer that forms on the internal metal substrate. On the other hand, the chloride ion produces a certain amount of hydration energy, which is adsorbed

on the surface of the metal easily and replaces the oxygen into the chlorination layer, in which insoluble oxide becomes soluble chloride, making the surface go from a passivation state into an activated surface, which causes the metal to be destroyed. The simple epoxy resin coating without the addition of metal oxide was corroded by chloride ions quickly, which enters through micropores of the metal surface. Subsequently due to the electrochemical reaction the coating was broken, and the salt fog produced without metal oxide coating shows the pitting corrosion in the metal substrate.

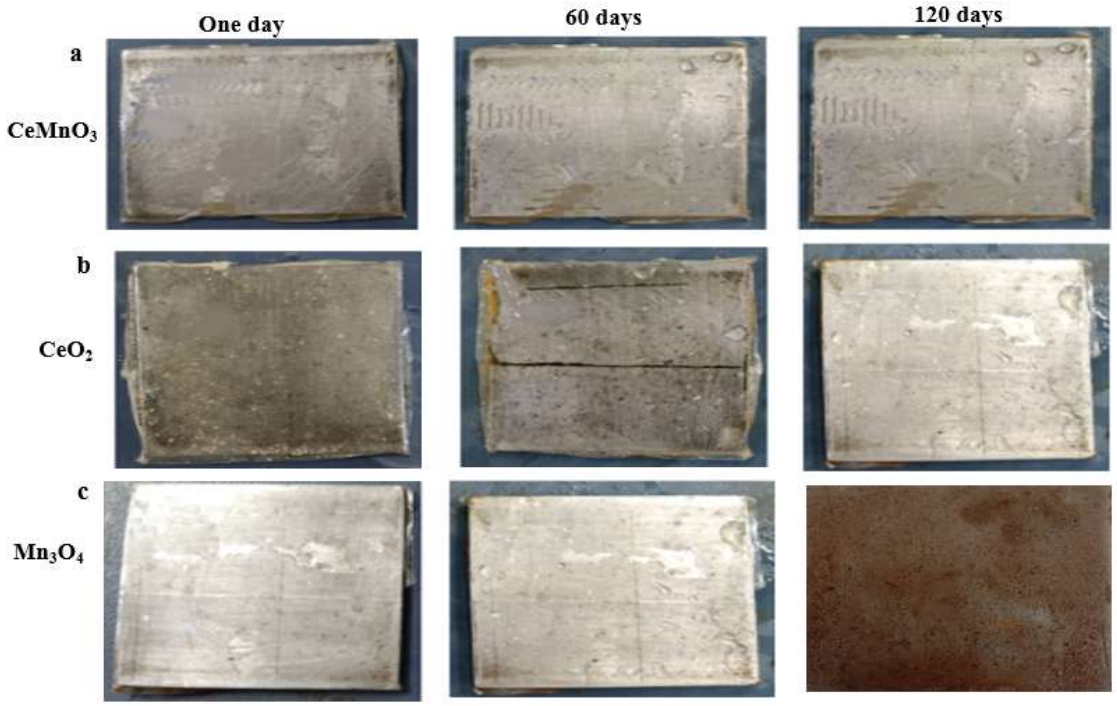

Figure 10.24 *Macro photographs of a) Ce-MnO_3, b) CeO_2, and c) Mn_3O_4 during salt-spray corrosion for day (1,60 and 120)*

10.5.3 Marine water corrosion

The corrosion behavior of $CeMnO_3$, CeO_2, and Mn_3O_4 in marine water collected from the Indian Ocean, Rameshwaram, were analyzed, and photographs were taken periodically **(Figure 10.25 a-c)**. After 120 days, the mild steel substrates show different corrosion phenomena. $CeMnO_3$ portion displays the corrosion products in the left-up corner. Iron oxides, or hydroxides, are responsible for the orange-brown color. The metal corrosion on the steel involves several steps, represented by the oxidation and reduction equation (**Eq.10.6 and 10.7**) and the overall redox reaction (**Eq.10.8**).

Oxidation

$$Fe \rightarrow Fe^{2+} + 2^{e-} Fe^{2+} \rightarrow Fe^{3+} + 2^{e-} \quad \textbf{(Eq.10.6)}$$

Reduction

$$O_{2(g)} + 2H_2O + 4^{e-} \rightarrow 4OH^- \quad \textbf{(Eq.10.7)}$$

$$2Fe^{2+}(aq) + \frac{1}{2}O_2(g) + 3H_2O \rightarrow 2FeOOH + 4H^+ \quad \textbf{(Eq. 10.8)}$$

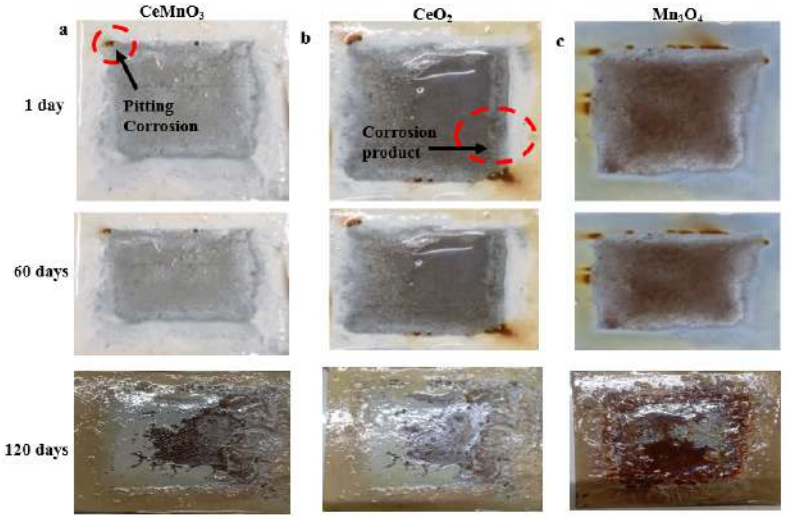

Figure 10.25 *a) macro photographs of a) $CeMnO_3$ b) CeO_2, and c) Mn_3O_4 in saltwater corrosion using marine water for 1st day to 120 days.*

CeO_2 **(Figure 10.25a)** part illustrates the pitting corrosion ascribed to the under dense adhesive tape. There is no evidence of corrosion products or cracking in composite metal oxide coatings. After a few days, corrosion occurs in steel due to the access of Cl^- ions from the solution. Chloride ions, O_2, and H_2O molecules could penetrate through the epoxy coating; degradation occurs, and hence the stability and durability of the coating will be measured. Compared to all synthesized metal oxides, it is challenging for chloride ions to enter through the $CeMnO_3$ layer.

Incorporating nano metal oxides upsurges the diffusion resistance on the surface of the coating layer. After a stipulated time, small molecules like water, oxygen, and a few anionic species will enter through the coating breakage. The rupture of metal oxide coatings happened in a stepwise manner. Initially, the water molecule will enters the coating, followed by the dispersion of Cl^- ions. The zig-zag pathway of metal oxide permits

chloride ions to occupy the site at the coating and steel surface. The electron affinity of the composite metal oxide attracts more electrons and urges the cathodic reaction to complete the degradation reaction. The $CeMnO_3$ film shows excellent adhesive properties and mechanical strength. Mn oxide (620000 S/m) has high electrical conductivity than Ce oxide (140000 S/m), which is responsible for better performance . Moreover, the composite metal oxide will trap and hamper all the threatening ions within the corrosive environment and hence have superior action. Compared to CeO_2, Mn_3O_4, mixed metal oxide provides mechanical strength to the coating, and the pervasion of moisture was diminished. The mechanism of physical adsorption behavior of $CeMnO_3$ is shown in **Figure 10.26a**.

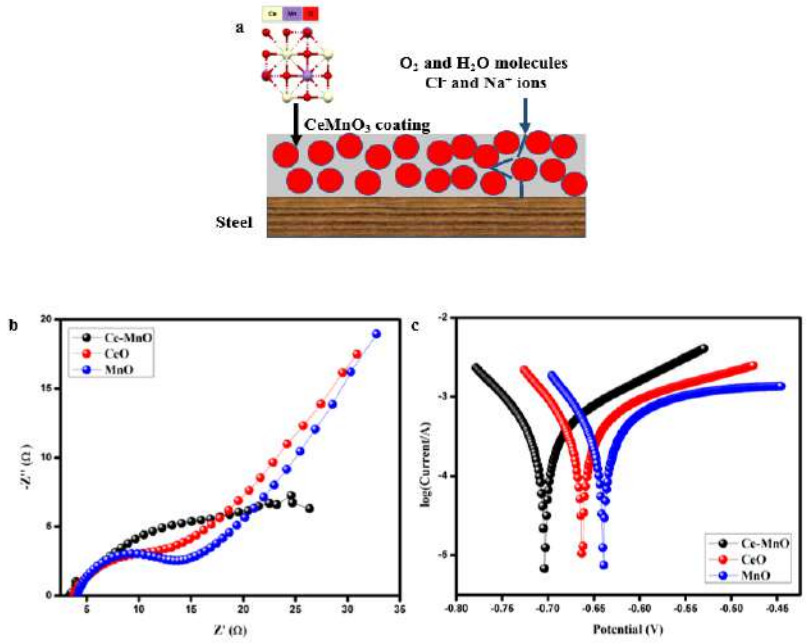

Figure 10.26 *a) Proposed mechanism for the action of $CeMnO_3$ coating on a steel surface and b) Nyquist plot and c) polarisation curves of $CeMnO_3$, CeO_2, and Mn_3O_4.*

10.5.4 Electrochemical studies

10.5.4.1 Nyquist Plot

The Nyquist plot for the steel in 3.5 wt-% NaCl solution were examined and shown in **Figure 10.27,** in which a capacitive loop at higher frequency is due to the charge transfer. The thickening of the protective layer is caused by the decreasing C_{dl} values, while the increasing R_{ct} values represent the behavior of steel, which protects the mild steel.

ii) Effect of immersion time on corrosion behaviors

The effect of immersion time on the protective performance of nanocomposite coating has been investigated in 3.5 wt-% NaCl solution. The Nyquist diagrams obtained for $CeMnO_3$, CeO_2, and Mn_3O_4 nanocomposite at different immersion times (Blank,3, 9, and 24 h) are represented in **Figure 10.27** and the fitting values are given in **Table 10.14**. It can be seen clearly that for blank and epoxy-$CeMnO_3$/CeO_2/Mn_3O_4, resistances decrease with increasing immersion time from 3 h to 24 h, the electrolyte can find more paths through the epoxy of metal nanocomposite film to the mild steel surface and the rate of charge transfer between the mild steel and the solution interface increases, and hence the corrosion resistance decreases. After 24 h, as corrosion products lead to a closing of the pores, the corrosion resistance does not show significant change. In which the blank with epoxy coating surface is slightly corroded. However, the surface of steel with epoxy nanocomposite coating shows no corrosion and is free from rust. when comparing the epoxy-$CeMnO_3$/CeO_2/Mn_3O_4 the highest efficiency in epoxy-$CeMnO_3$ indicated that the electron affinity of the composite attracts more electrons in the cathodic reaction to complete degradation so it was found to be high mechanical strength.

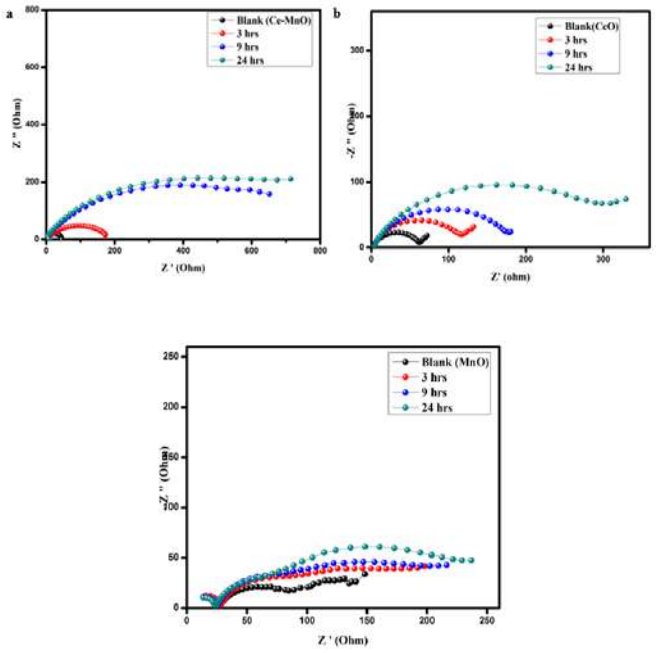

Figure 10.27 *Effect of immersion time on corrosion behaviors in a)$CeMnO_3$, b)CeO_2, and c) Mn_3O_4*

Table 10.14 *Nanocomposite concentration at different immersion time in 3.5 wt% NaCl solution*				
Metal oxide	**Immersion time**	**R_{ct}(MΩ cm^2)**	**C_{dl} (µF cm^2)**	**IE (%)**
$CeMnO_3$	**BLANK**	20.77	19.5	
	3	38.55	19.2	46.11
	9	57.26	18.8	63.71
	24	67.11	17.8	69.04
CeO_2	**BLANK**	19.49	24.8	
	3	27.84	20.9	30.00
	9	51.43	20.0	62.10
	24	78.52	19.8	75.18
Mn_3O_4	**BLANK**	17.9	43.2	
	3	23.4	39.0	23.5
	9	36.5	35.6	50.95
	24	57.01	30.6	68.6

10.5.4.2 Electrochemical property

The corrosion inhibition activity of epoxy-$CeMnO_3$/CeO_2/Mn_3O_4 film was examined by polarization study in a 3.5 wt-% NaCl solution in an air (**Figure 10.26c** & **Table 10.15)**. Greater E_{corr} and lower I_{corr} are the main characteristics of anti-corrosion activity, and composite metal oxide fixes very well in this range . But CeO_2 has the opposite behavior, and hence it has poor adhesion. Accordingly, we conclude that composite metal is the preferable anti-corrosion material instead of individual metal oxide. The shift in E_{corr} infers the mixed type of inhibition due to its protective mechanism on both H_2 evolution and metal displacement. The anodic part displays the inflection points at positive potentials with varied slopes signifying a barrier effect.

ii) Anti-corrosive performance of the three coatings

To compare the effect of anticorrosive properties of $CeMnO_3$, CeO_2, and Mn_3O_4, which have been deposited on mild steel. CeO_2 and Mn_3O_4 coating shows higher and lower corrosion protection compared to $CeMnO_3$ coatings, respectively. In which CeO_2, and Mn_3O_4 the microparticles can be placed into free spaces of the polymer matrix and prevent corrosive species from reaching the mild steel surface, hence $CeMnO_3$ showed better anti-corrosive behavior compared other two. On the other hand the smaller size and larger aspect ratio of nanoparticles in reasonable to lead to the better distribution of nanoparticles in $CeMnO_3$ and lower porosity of coating, and thus, better anti-corrosive properties.

Table 10.15 *Electrochemical parameters for nanometal oxides.*

Composition	E_{corr} / V	I_{corr} /A cm^{-2}	Rp/Ω cm^2
$CeMnO_3$	-551	131	145
CeO_2	-599	486	62.7843
Mn_2O_3	-573	380	64.7874

10.6 CONCLUSION

In this chapter we examines a series of divalent metal ions like Mn^{2+}, Co^{2+}, Ni^{2+}, Cu^{2+}, Zn^{2+}, Cd^{2+}, Mg^{2+}, Ca^{2+}, Sr^{2+}, Ba^{2+} with 2- naphthoic acid and guanidine in a methanolic medium. The prepared complexes were characterized by element analysis, FTIR, electronic spectra, thermal analysis, and P-XRD. The complexes reveal good antimicrobial and antioxidant activity against Zn (II) ions.

The photometric properties of the complexes were studied by PL analysis, The nickel shows a high excitation peak comparable with the other two compounds due to metal to ligand charge transfer. The fluorescence lifetime can be calculated from the metal complexes is 441,530 μs and 450 μs in which R^2 values were calculated. The CIE value was closely related to the NTSC of standard which results in the blue phosphors emitted which gather in the near Understanding *Ultraviolet LED*-based White-LEDs. The metal complex's Duv values occur around -0.0049 to -0.175 in which the negative Duv value is

closely related to the white light emission. Ni (II)complexes in TLCI=100 which requires the light source observed in television were as the Co (II)and Cu (II) produce TLCI=1 they are not suitable in applications in the broadcast area. ΔE* value always produces the positive it understood they are considered in commercial production. The evidence established the newly exposed efficient metal complexes have great application towards the blue-light-excited w-LEDs found to be suitable phosphors for OLEDs.

On otherhand to study the corrosion behavior, on the nanometal and mixed metal oxide namely $CeMnO_3$, CeO, and MnO was synthesized and coated with epoxy resin on the steel substrate. The structural parameters and surface morphology were determined from XRD, SEM, and TEM analysis.We have successfully analyzed the anti-corrosion behaviour epoxy- $CeMnO_3/CeO_2/Mn_3O_4$ in different mediums like salt-spray and marine water. The encapsulated nanocomposites material prevents the steel plate for 120 days by forming insoluble protective layer. In electrochemical corrosion studies, $CeMnO_3$ possesses a higher E_{corr} value demonstrating its enhanced protection ability. CeO_2 shows minimum anti-corrosion behavior due to higher affinity and lower diffusivity of trivalent ion than divalent manganese oxide. Thus, effectiveness in mitigating membrane degradation will be poor in cerium oxide, so this can be concluded that all the synthesized epoxy metal oxides have suitable barrier properties against corrosive environments.

REFERENCES

1. Siva, V. *et al.* A promising guanidinium based metal-organic single crystal for optical power limiting applications. *Chinese J. Phys.* **64**, 103–114 (2020).
2. Wang, G. H., Li, Z. G., Jia, H. Q., Hu, N. H. & Xu, J. W. Metal–organic frameworks based on the pyridine-2,3-dicarboxylate and a flexible bispyridyl ligand: syntheses, structures, and photoluminescence. *CrystEngComm* **11**, 292–297 (2009).
3. Singh, L. J. & Singh, R. K. H. Synthesis and photophysical properties of new Ln(III) (Ln = Eu(III), Gd(III), or Tb(III)) complexes of 1-amidino-O-methylurea. *Chem. Pap.* **68**, 223–232 (2014).
4. Ji, C. *et al.* Synthesis and photoluminescence properties of a novel BaGe4O9:Eu3+ red emitting phosphor for warm white LEDs. *Dye. Pigment.* **160**, 772–778 (2019).
5. Lou, Z. & Hao, J. Cathodoluminescence of rare-earth-doped zinc aluminate films. *Thin Solid Films* **450**, 334–340 (2004).
6. Mondal, S., Dinda, D., Shaw, B. K. & Saha, S. K. Tunable Color in 2,6-Diaminopyridine-Functionalized Graphene Oxide. *J. Phys. Chem. C* **120**, 11085–11091 (2016).
7. Ohno, Y. Practical Use and Calculation of CCT and Duv. *http://dx.doi.org/10.1080/15502724.2014.839020* **10**, 47–55 (2013).
8. Davis, W. & Ohno, Y. Approaches to color rendering measurement. *https://doi.org/10.1080/09500340903023733* **56**, 1412–1419 (2009).
9. Böhler, P., Emmett, J. & Roberts, A. Toward a ‘standard’ television camera color model. *SMPTE Motion Imaging J.* **122**, 30–36 (2013).
10. Ly, B. C. K., Dyer, E. B., Feig, J. L., Chien, A. L. & Del Bino, S. Research Techniques Made Simple: Cutaneous Colorimetry: A Reliable Technique for Objective Skin Color Measurement. *J. Invest. Dermatol.* **140**, 3-12.e1 (2020).
11. Houser, K., Mossman, M., Smet, K. & Whitehead, L. Tutorial: Color Rendering and Its Applications in Lighting. *LEUKOS - J. Illum. Eng. Soc. North Am.* **12**, 7–26 (2016).

12. Hu, X. *et al.* Study of Color Rendering Evaluation Method of Light Sources for Printing Matter. *IEEE Access* **8**, 5526–5536 (2020).

13. Arunadevi, N. & Vairam, S. 3-hydroxy-2-naphthoate complexes of transition metals with hydrazine-preparation, spectroscopic and thermal studies. *E-Journal Chem.* **6**, (2009).

14. N, A., S, D. & S, V. The acid adducts hydrazinium 2-hydroxybenzoate-2-hydroxybenzoic acid (1/1) and hydrazinium 3-hydroxy-2-naphthoate-3-hydroxy-2-naphthoic acid (1/1). *Acta Crystallogr. C.* **68**, (2012).

15. Devipriya, S., Arunadevi, N. & Vairam, S. Synthesis and thermal characterization of lanthanide(III) complexes with mercaptosuccinic acid and hydrazine as ligands. *J. Chem.* (2013) doi:10.1155/2013/497956.

16. Mahdavi, M., Ghani, K. & Nosratzadegan, K. Synthesis, Structural and Energetic Properties of Copper(II) Perchlorate Complex with Aminoguanidine. *Zeitschrift für Anorg. und Allg. Chemie* **643**, 1771–1775 (2017).

17. Belkhir-Talbi, D. *et al.* Synthesis, characterization, theoretical studies, ADMET and drug-Likeness analysis: Electrochemical and biological activities of metal complexes of 3-(2-hydroxybenzoyl)-2H-chromen-2-one. *J. Mol. Struct.* **1179**, 495–505 (2019).

18. Singh, P., Singh, R. B. & Singh, J. Bioinspired triangular ZnO nanoclusters synthesized by Argyreia nervosa nascent leaf extract for the e ffi cient electrochemical determination of vitamin C †. 25752–25763 (2021) doi:10.1039/d1ra04704c.

19. Kumar, H., Sharma, R., Yadav, A. & Kumari, R. Synthesis , characterization and influence of re duce d Graphene Oxide (rGO) on the performance of mixed metal oxide nano-composite as optoelectronic material and corrosion inhibitor. *Chem. Data Collect.* **29**, 100527 (2020).